JOINT EUROPEAN TORUS

JET–P(91)16

H. Weisen, H. Bergsaker, D. Campbell, S.K. Erents, L. de Kock,
G. McCracken, M. Stamp, D. Summers, P. Thomas, M. von Hellermann,
J. Zhu and JET Team

Boundary Ion Temperatures in JET

Boundary Ion Temperatures in JET

H. Weisen[1], H. Bergsaker[2], D. Campbell, S.K. Erents[3], L. de Kock,
G. McCracken[3], M. Stamp, D. Summers, P. Thomas, M. von Hellermann, J. Zhu[3]
and JET Team*

JET-Joint Undertaking, Culham Science Centre, OX14 3DB, Abingdon, UK

[1]CRPP, Association Euratom-Confederation Suisse, Lausanne, Switzerland.
[2]Manne Siegbahn Institute of Physics, Stockholm, Sweden.
[3]AEA Fusion, Culham, Abingdon, Oxon, UK.
** See Appendix 1*

Preprint of Paper to be submitted for publication in
Nuclear Fusion

Boundary Ion Temperatures in JET

H Weisen[1], H Bergsaker[2], D Campbell, S K Erents[3], L de Kock, G McCracken[3], M Stamp, D Summers, P Thomas, M von Hellermann, J Zhu[3]

JET Joint Undertaking, Abingdon, OXON OX14 3EA, UK

permanent addresses:

[1] CRPP, Association Euratom-Confédération Suisse, 21 avenue des Bains, 1007 Lausanne, Switzerland

[2] Manne Siegbahn Institute of Physics, 10405 Stockholm, Sweden

[3] AEA Fusion, Culham, Abingdon, OXON OX14 3EA, UK

Abstract. Ion and electron temperatures of up to 5 keV have been obtained within 10 cm of the last closed flux surface (LCFS) in hot-ion H-modes with 18 MW of NBI heating. The ion temperature profiles appear to have 'pedestals' which scale with power per particle, $T_i(a) \leq P(a)/n_e(0.9a)$ [keV, MW/10^{19} m^{-3}], in H-modes. In L-modes pedestal temperatures are an order of magnitude lower. This difference can be explained by the one order of magnitude difference in particle residence time in the two confinement modes. In H-modes, the resulting pressure 'pedestals', contribute typically 40%, and up to 5 MJ, to the plasma stored energy, explaining about half of the confinement improvement over L-mode conditions. The remaining improvement occurs across the entire plasma, but most notably in the periphery. There is ample evidence that ions with energies in the keV range escape to and beyond the LCFS, and account for most of the loss power in the ion channel. It includes results from energy discriminating probes in the scrape-off layer and the analysis of the characteristics of the heat strike zones in the X-point configuration. The observed boundary ion temperatures have far reaching implications for fusion reactivity, power handling, wall erosion and impurity production in reactor conditions. They suggest that it is possible to bring the entire volume of a reactor plasma to thermonuclear temperatures, with a considerable boost to the overall thermonuclear reactivity.

I) Introduction

The primary goals of controlled nuclear fusion research include the improvement of the energy confinement and the control of boundary conditions. Conditions at the boundary determine particle and impurity influxes and outfluxes, heat deposition and edge radiation losses. They can also have a significant direct influence on global energy confinement, as demonstrated by the high confinement mode (H-mode), which brings an improvement of typically a factor of 2 over 'normal' L-mode confinement. Soon after its discovery, the H-mode was associated with a narrow transport barrier at the plasma edge, where steep density and temperature gradients develop[1-3]. Early results from the ASDEX tokamak showed H-mode profiles with T_e increasing from about 20 eV to 500 eV within 2 cm of the separatrix, while over the same distance the plasma density increased by an order of magnitude[2].

The results we present show that in JET H-modes ion temperatures in the keV range are found to within only 4 to 10 centimetres inbound from the last closed flux surface (LCFS). Since this is only a few poloidal ion Larmor radii, significant ion orbit losses, with keV escape energies have to be expected. Evidence that energetic ions escape into the scrape-off layer, and are responsible for most of the heat flux in the ion channel, is available at JET from a variety of measurements. They include results from ion energy probes in the scrape-off layer and from ion implantation profiles in nickel samples, and measurements of the characteristics of heat strike zones on the X-point target plates. Heat strike zones with a very high ratio of power to particle flux, indicating particle energies of a few keV, have been observed during H-modes in JET. Similar evidence, although with lower ion temperatures (or energies), was obtained in limiter plasmas from measurements using Langmuir probes in the limiters. The calorimetrically measured heat flux to the limiters could only be explained if ion temperatures at the LCFS were assumed to be substantially higher than the local electron temperature, and comparable to spectroscopically measured ion temperatures in the vicinity of the LCFS [4,5]. Evidence of ions with energies well above the local electron temperature in the scrape-

off layer has been available for a long time from various probe techniques[6-16]. However only recent spectroscopic measurements inside the LCFS, have shown the boundary ion temperatures to be sufficiently high to explain the probe results in terms of particles escaping from the thermal population just inside the LCFS.

The observations also show that across the few outermost cm of the cross-section, ions and electrons must behave very differently, probably as a result of the large difference in poloidal Larmor radius. Unlike the electrons, which clearly have scrape-off temperatures of tens of eV, the ions appear to be unable to establish a thermal gradient (at least in the strict sense of a local temperature as a Maxwellian velocity distribution) across a boundary layer of width comparable to their orbit width The evidence suggests a picture of the scrape-off layer and transport barrier region where energetic ions escaping from the main plasma coexist, out of thermal equilibrium, with a probably denser population of lower energy ions created by fuel ionisation, recycling and sputtering.

The content of this contribution can be broadly outlined as follows. In section II we present charge exchange spectroscopy measurements showing that the ion temperature does not, within an effective resolution of a few cm, decrease to zero as the LCFS is approached. One consequence of existence of such a 'pedestal' is its considerable contribution to the stored energy, as shown for an example of a hot-ion H-mode. In section III we show that pedestal temperatures scale with power per particle, an observation which can be understood from the relationship between particle and energy losses at the boundary. Evidence for escaping particles, from probe measurements in the scrape-off layer, and from the behaviour of the heat strike zones at the X-point tiles, is presented in section IV. Orbit losses are estimated and discussed in section V, especially in relation with the observation of a negative electric field in H-mode transport barrier region of several tokamaks and recent H-mode theories. The pedestal contribution to the stored energy is investigated in a confinement study presented in section VI. In H-modes the pedestal contributes typically 40% of the stored energy. The remaining improvements occur across the cross-section, but most noticeably

in the periphery. Similarly, we show in section VII, that the pedestal ion temperature and pressure make a considerable contribution (40-70% in H-modes) to the overall fusion performance, as measured by the volume average deuteron pressure squared.

II) Charge exchange measurements of ion temperature near the plasma boundary.

A remarkable feature of ion temperature profiles measured at JET for a large variety of heating conditions and plasma configurations is that they all exhibit a fairly monotonic gradient over the last 40 or more cm of the minor radius, and then appear to end abruptly with a marked 'pedestal' near the last closed flux surface (LCFS). Examples of such ion temperature profiles measured using the active charge exchange spectroscopy (CXS) diagnostic[17,18] are shown in fig.1. They range from near ohmic conditions to high performance H-mode discharges with 18 MW of neutral beam heating and central ion temperatures in excess of 25 keV. The position of the LCFS was obtained from the equilibrium reconstruction using magnetic measurements. In some of the high performance discharges obtained in 1990 ion temperatures of up to 11 keV were obtained within 21 cm of the LCFS (fig.1a). Unfortunately measurements within 10 cm of the LCFS were not available for these cases, due to an accidental misalignement of the CXS viewing system, possibly as a result of a heavy disruption. An example of a charge exchange spectrum of CVI obtained from a viewing volume 21 cm from the LCFS is shown in fig.2 and exhibits a clear Gaussian shape over three thermal widths, corresponding to 11 keV.

In two of the examples of fig.1 the plasma was swept in major radius, allowing the fixed viewing volumes of the CXS diagnostic to provide a complete coverage of the minor radius. We used these measurements in an attempt to obtain an estimate of the

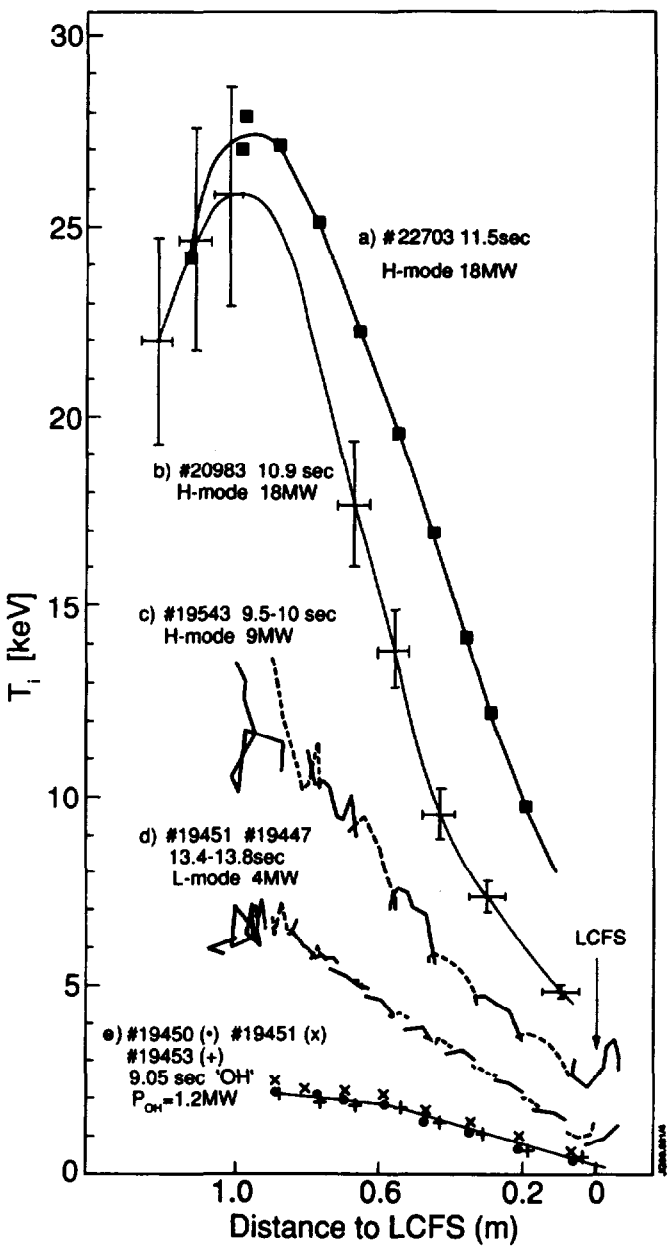

Fig.1 Ion temperature profiles from charge exchange spectroscopy in double-null X-point discharges.

a) I_p = 4.2 MA, B_T = 2.8 T, $\langle n_e \rangle = 2 \cdot 10^{19}$ m^{-3}, $T_e(0)$ = 9 keV, P_{NBI} = 18 MW.
b) I_p = 4.1 MA, B_T = 2.8 T, $\langle n_e \rangle = 3 \cdot 10^{19}$m^{-3}, $T_e(0)$ = 9 keV, P_{NBI} = 18 MW.
c) I_p = 3 MA, B_T = 2.8 T, $\langle n_e \rangle = 2.5 \cdot 10^{19}$m^{-3}, $T_e(0)$ = 7.5 keV, P_{NBI} = 9 MW.
d) I_p = 3 MA, B_T = 2.8 T, $\langle n_e \rangle = 2.0 \cdot 10^{19}$m^{-3}, $T_e(0)$ = 5.5 keV, P_{NBI} = 4 MW.
e) as d), but obtained within 50ms of application of NBI. P_{OH}=1.2 MW.

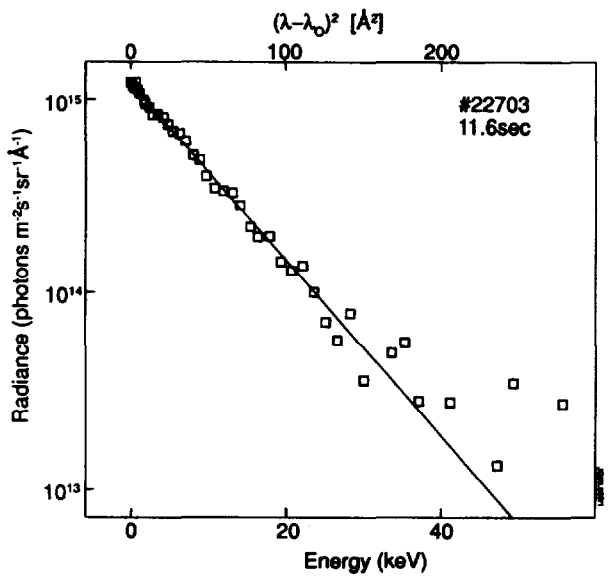

Fig.2 Charge exchange line profile obtained 21 cm inside LCFS. Line used was CVI 8→7, λ=529 nm. T_i=11 keV.

scale length of the very steep ion temperature gradients we suspected to exist at the LCFS (fig.3). The viewing geometry for the outermost viewing volume is shown in fig.3d. Although the nominal resolution of the system was only ±7 cm, the effective resolution can be much less if there is only a small overlap with the plasma. We see that, although the signal from the charge exchange line drops to 5% of its maximum value as the overlap reduces to zero, the inferred ion temperature is never seen to drop to zero. The small signal which is still observed when the active viewing volume is outside the LCFS is really picked up inside the LCFS, along the line of sight, and corresponds to emission from CVI in the edge plasma, excited by electron impact or resulting from charge exchange reactions with background neutrals[19]. From the temperatures obtained for this emission, which are somewhat higher than the lowest values obtained when the active CX signal dominates, we deduce that it originates from about 10 cm inside the LCFS. It is also observed in purely ohmic discharges, and in the case of fig.1e, was characterised by a temperature of 0.8 keV. Unfortunately the presence of this small signal must be expected to mask the active CX signal from a viewing volume smaller than about 4 cm in radial extent near the LCFS as sketched in fig.3. The measurements do however show that the ion temperature remains high to at least as close as 4 cm from the LCFS. This is barely more than a thermal ion orbit width at 3 keV. The toroidal rotation induced by the injection of momentum by the heating beams is characterised by a similar 'pedestal', as shown on fig.3c.

The time evolution of the plasma parameters of an NBI heated high performance double-null X-point discharge is shown in figs. 4 and 5. The discharge underwent a transition to the H-mode at t=10.25 s, and attained a central fusion triple product $n_D(0)T_i(0)\tau_E$ of $9{\cdot}10^{20} keV m^{-3}$ s before the plasma was swamped by a sudden massive influx of carbon impurities at t=11 s (fig.4). Like most H-modes in JET, this discharge was characterised by a flat density profile with a sharp gradient within the last 5 cm of the LCFS[20].

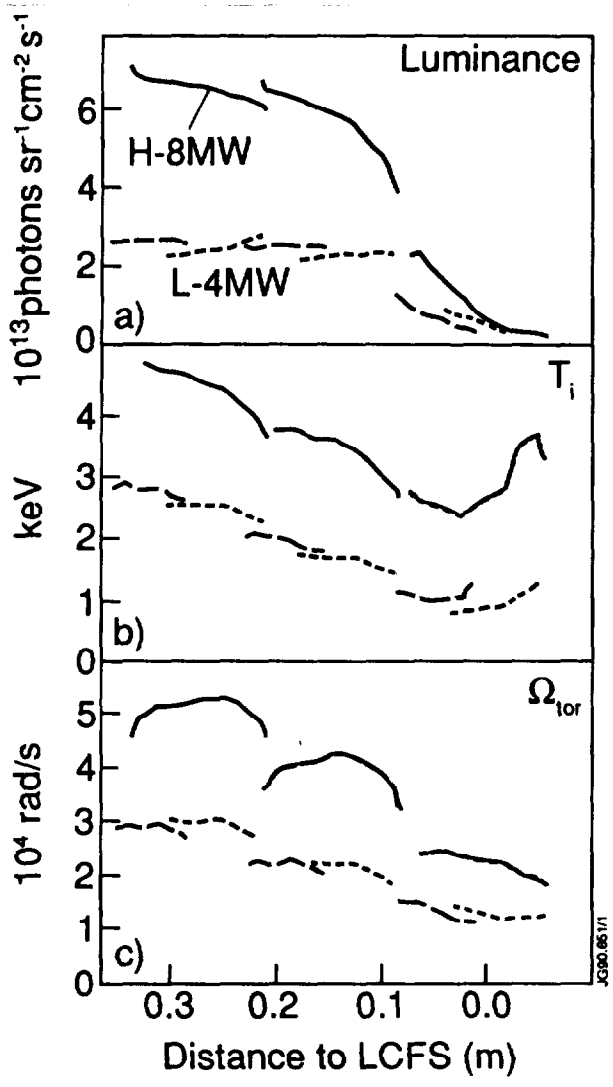

Fig.3 Sweeping of LCFS accross viewing volume of charge exchange spectroscopy diagnostic.

a) Charge exchange line intensity (CVI).

b) Ion temperature. Note apparent increase beyond LCFS is due to weak background emission along line of sight.

c) Angular frequency of toroidal rotation.

d) Geometry of sweeping experiment.

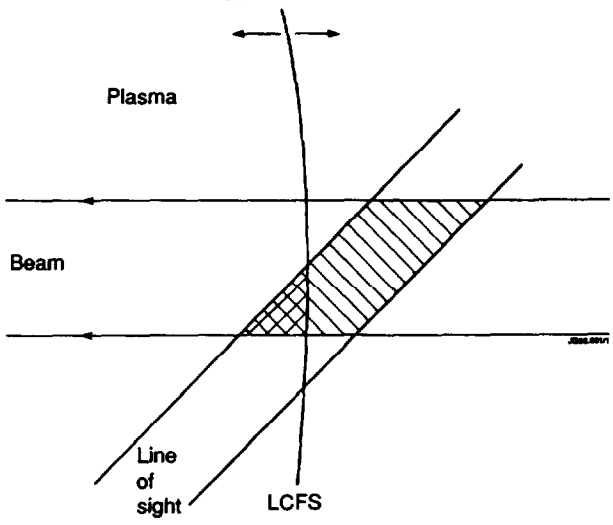

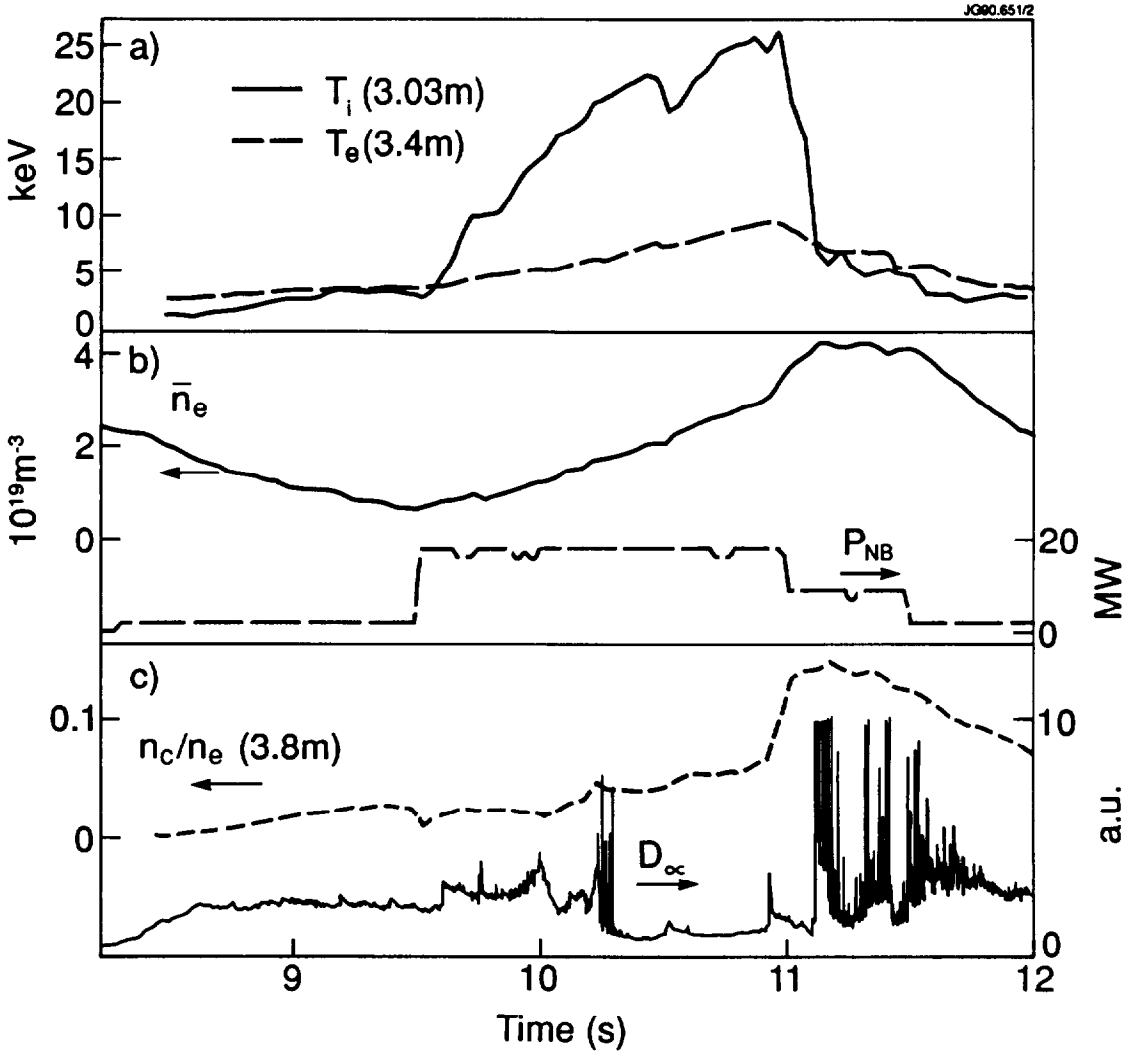

Fig.4 Evolution of plasma parameters in a high performance discharge (#20983).

a) Core ion and electron temperatures.

b) Average electron density and neutral injection power.

c) D_α line signal indicating a transition to the H-mode at 10.25 s, and carbon concentration 25 cm inside LCFS, from CXS.

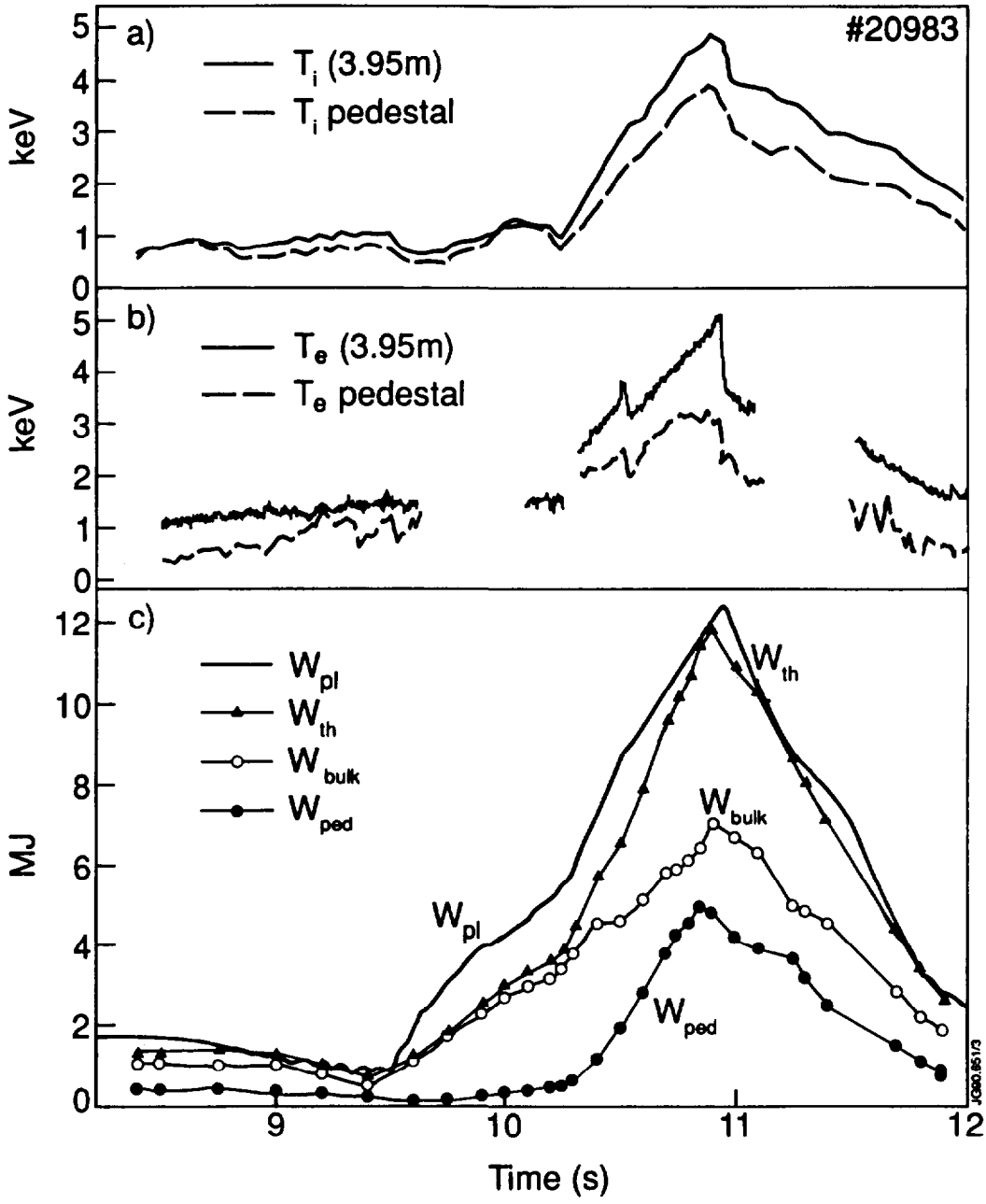

Fig.5 Evolution of edge ion (a) and electron (b, from ECE) temperatures in discharge #20983. The dotted lines are extrapolations to the LCFS. The blanked sections in the ECE data are due to nonthermal emission produced by ELMs.

c) Evaluation of pedestal contribution to the total stored energy. W_{ped} is as defined in eq.(1). W_{th} is the total volume integrated ion and electron thermal energy. Ion density was evaluated from electron density measured by FIR interferometer and CXS measurement of carbon impurity density. At 10.9 s total thermal ion energy was 6.5 MJ, total electron energy was 5 MJ. $W_{bulk} = W_{th} - W_{ped}$. W_p is the plasma stored energy from equilibrium reconstruction. The difference between W_p and W_{th} is due to unthermalised beam ions (~1.9 MJ at 10 s, ~ 1MJ at 10.9 s).

During the H-mode ion and electron temperatures measured near the edge at a major radius of 3.95 m increase from about 1 keV to 5 keV (fig.5 a&b). We can define pedestal temperatures by extrapolating from the two outermost available measurements to the LCFS, as illustrated in fig.6. They are shown as broken lines in fig.5, and range from below 1 keV in the L-mode to about 4 keV in this example. These values should not be taken as the true temperatures at the LCFS, which remain below our resolution.

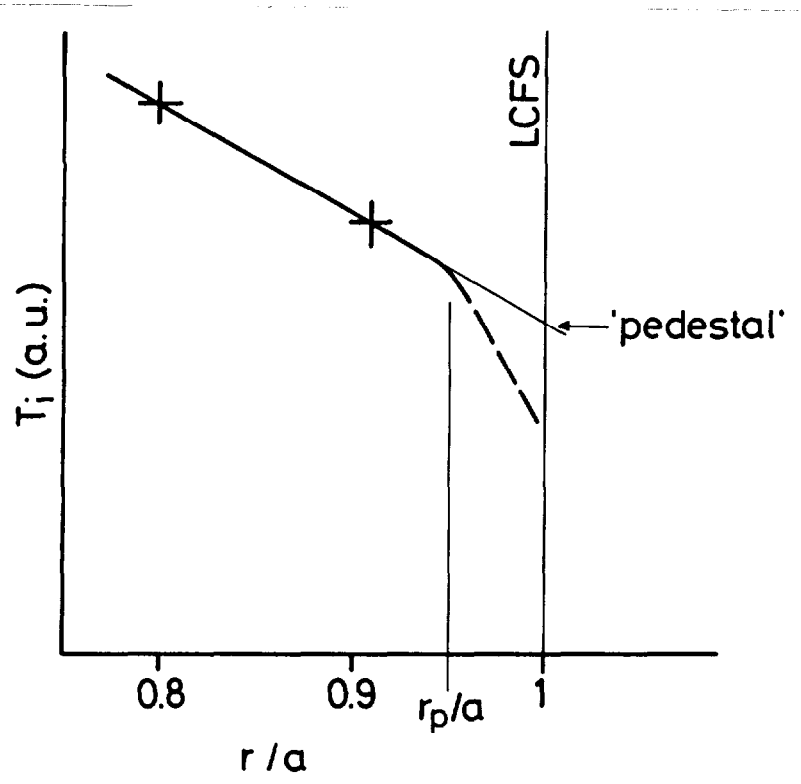

Fig.6 Shematic of ion temperature profile near the plasma edge. Crosses indicate typical CXS viewing positions. The steep gradient region for $r>r_p$, which is known to exist for electron density and temperature, is beyond the present resolution capabilities of the CXS diagnostic. The 'pedestal' temperature, as used in this paper, is defined by extrapolating the two outermost measurements to the LCFS, providing a lower bound approximation for $T_i(r_p)$.

We have conducted a number of checks to verify the consistency of ion temperature data from CXS with other measurements on JET. The volume integrated ion and electron thermal energies,

which depend sensitively on the edge parameters, were found to be in excellent agreement with the global plasma energy from the equilibrium reconstruction, or measured with a diamagnetic loop. The temperatures at the LCFS were taken to be equal to the above defined pedestals. The volume integrated ion-electron equipartition power was found to be in the range 2-6 MW for hot ion H-modes. Although large in some cases, this power is sustainable by the ions, given the available input power. It is however clear that the high boundary ion temperatures in the H-mode are only possible because electron temperatures are high enough throughout the discharge to allow the ions to decouple.

The abrupt steepening of the temperature and density gradients near the LCFS[20] indicates the existence of an edge transport barrier with vastly enhanced particle and energy confinement. It is instructive to define the contribution of the resulting pressure pedestal to the global energy confinement. We can define its contribution to the plasma stored energy as

$$W_{ped} = 3/2\ [V(r_p)p(r_p) + \int_{r>r_p} p(\underline{r})dV], \qquad (1)$$

where r_p is the minor radius beyond which the gradients steepen (fig.6), a the radius of the LCFS, $V(r_p)$ is the volume enclosed by the flux surface at r_p, and $p(r) = n_i(r)kT_i(r)+n_e(r)kT_e(r)$. W_{ped} is the plasma energy that would result if there was no confinement inside $r=r_p$. Due to the limited diagnostics resolution, the exact value of r_p is poorly known. However since $r_p \geq 0.95a$, we obtain a good approximation to the above expression by neglecting the second term on the RHS and using the pedestal values as defined above instead of those at r_p, together with the total plasma volume. For most of the data presented the pedestal density was taken from the Abel inverted far infrared interferometer data at $r \cong 0.9a$. In the example shown in fig.5c, the stored energy associated with the pedestals rises to nearly 5 MJ in the course of the H-mode, when it contributes up to 40% to the total stored energy. The present results confirm the conclusions of an earlier study[21,22], which was based on electron density and temperature measurements only, and assumed $T_i=T_e$.

The existence of an effective transport barrier in the H-mode leads to considerably broadened temperature and density profiles, as compared to their L-mode counterparts. This is illustrated in fig.7, where we compare H- and L mode profiles with the same central ion temperature. Each of the examples shown is one of the best performing (in terms of neutron production) in its mode of confinement. In the inner-wall limited L-mode case, despite the low edge density, the low edge electron temperature leads to a clamping of the ion temperature at the edge to about 1 keV. In the H-mode case the electron temperature 10 cm inside the LCFS is already 4.5 keV, which is sufficient to decouple the ions throughout the plasma volume.

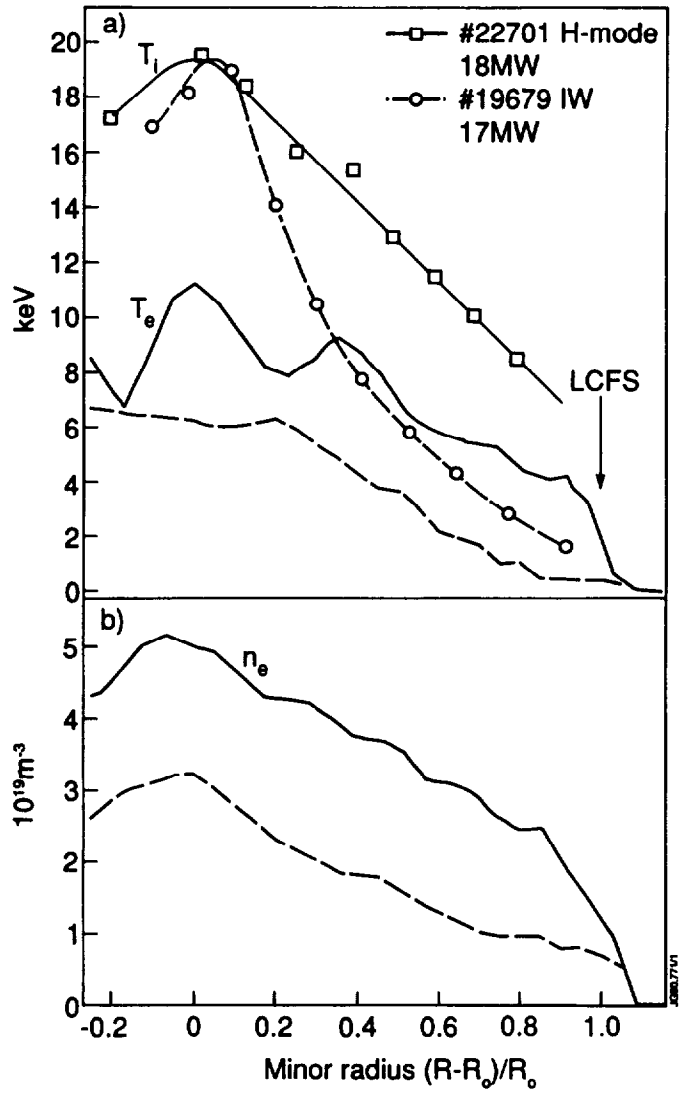

Fig.7 Comparison of temperature and density profiles in a hot ion limiter discharge and a hot ion H-mode discharge.

III) Scaling of boundary ion temperatures

The most important parameter in determining the boundary ion temperatures is found to be the power available per particle at the edge. Fig. 8 shows the edge ion temperature pedestals as defined in the previous section, as a function of $P(a) = P_{in} - dW_p/dt - P_{rad}$ in X-point discharges. To obtain a good estimate of the pedestal temperatures we only used data with profile measurements to within about 10 cm of the LCFS. In the best H-modes T_i pedestals scale like $T_i(r_p) \leq 1.3\ P(a)/n_e(0.9a)$ [keV, MW, $10^{19}m^{-3}$], up to 4 keV. In L-modes boundary ion temperatures scale weakly with $P(a)/n_e(0.9a)$ at low power per particle, and remain below 1.5 keV.

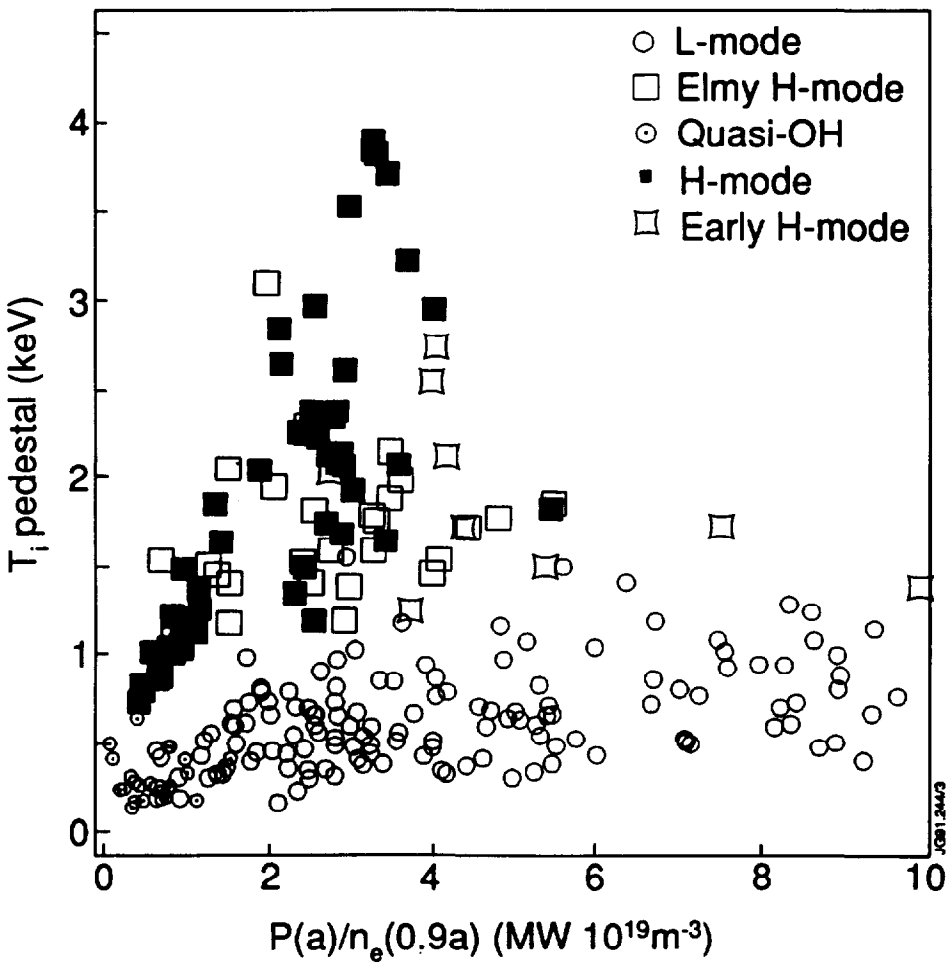

Fig.8 Boundary ion temperature scaling in the X-point configuration.

Discharges with pedestals larger than 3 keV resulted in the highest central fusion products ($n_D T_i(0)\tau_E$ up to $10^{21} keV m^{-3} s$), the highest neutron rates (up to $3.8 \cdot 10^{16} s^{-1}$) and the highest D-D fusion yields (up to $2.5 \cdot 10^{-3}$) obtained in JET up to date[23]. With edge ion collisionalities $\nu^*_{ii} = \varepsilon^{-1.5} R_0 q_a \nu_{ii}/v_i$ of order 10^{-1}, these plasmas are collisionless throughout the discharge. (ε is the inverse aspect ratio, R_0 the major radius, q_a the cylindrical safety factor, ν_{ii} and v_i the ion collision frequency and thermal velocity for $T_i(r_p)$).

The lowest edge ion temperature pedestals (~0.7 keV) in the H-mode were obtained with 8 MW of NBI and heavy gas puffing, raising the edge density $n_e(0.9a)$ to up to $9 \cdot 10^{19} m^{-3}$. These plasmas have collisional boundaries, $\nu^*_{ii} \sim 10$. Pedestals of a few hundred eV even exist in ohmic conditions. This is inferred from CXS measurements obtained within 50 ms of the beginning of NB heating, before the ion temperature profiles have changed appreciably.

Since the pedestals observed evolve during an H-mode we have attempted to distinguish between early H-modes (characterised by a high dW_p/dt), quiescent and elmy phases, shown with different symbols in fig.8. No attempt has been made to investigate the effects of different types of ELM's. Interestingly most elmy discharges have edge ion temperatures comparable to their elm-free counterparts.

In limiter discharges a very consistent scaling, with $T_i(a) \approx 0.13\ P(a)/n_e(a)$ [keV, MW, $10^{19} m^{-3}$], up to about 1 keV, is observed (fig.9). There was no measurable difference when the plasma was limited on the graphite inner wall, on graphite limiters or on beryllium belt limiters. In the former two cases the CXS measurements were obtained from a CVI line at 529 nm, whereas in the latter they were based on a BeIV line at 468 nm. As in the X-point case, measurements obtained within the first 50 ms after the beginning of NBI show that pedestals also exist in ohmic plasmas. Corroborating evidence has been obtained in limiter discharges from passive spectroscopy and from Langmuir probe and calorimetric measurements.

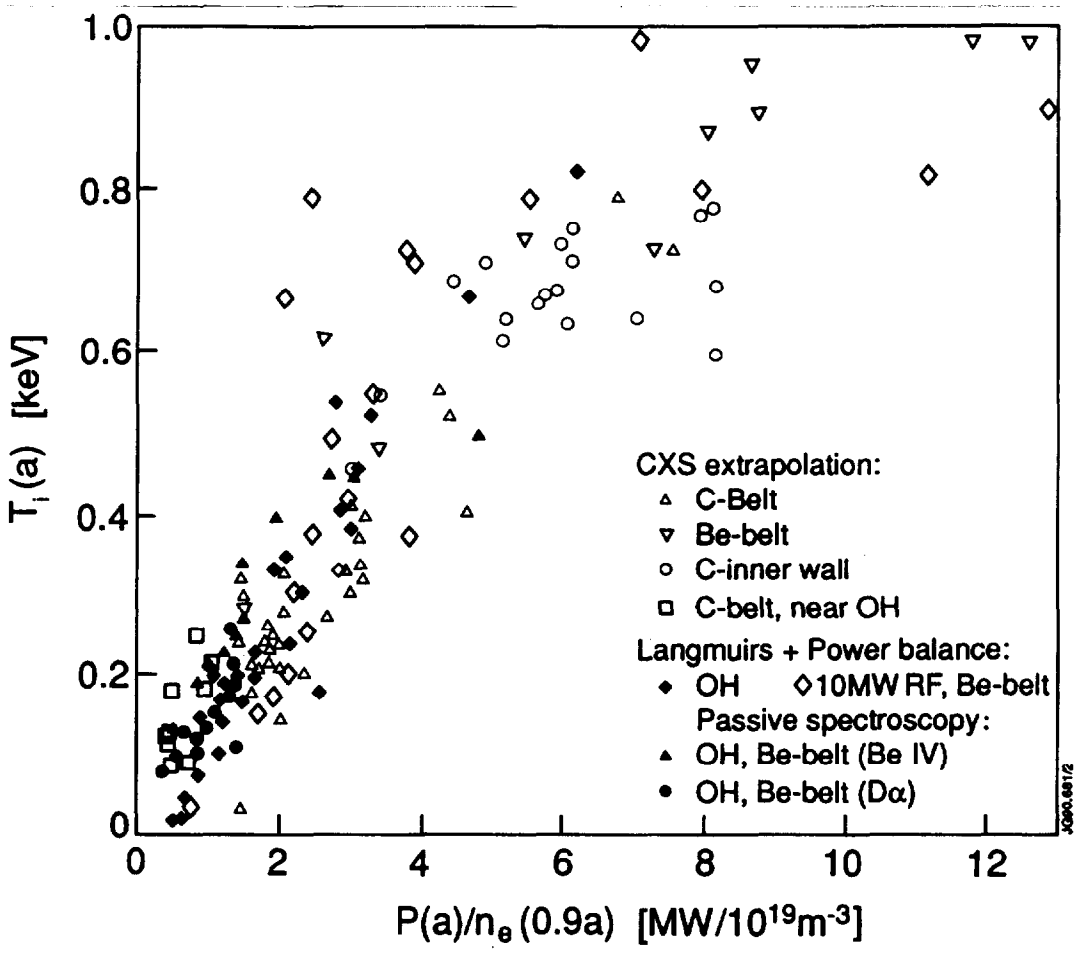

Fig.9 Boundary ion temperature scaling in limiter configurations.

The earliest evidence in JET of energetic ions at the LCFS, has come from measurements of particle flux density and electron temperature using fixed Langmuir probes in the beryllium belt limiters in conjunction with calorimetric measurements of the power to the edge by thermocouples built into the limiters[4]. It was found that the power to the edge inferred from the probe measurements could not account for the power to the limiters if $T_i=T_e$ was assumed. An ion temperature substantially higher than the electron temperature had to be postulated in order to obtain agreement. The ion temperatures so inferred are shown in fig.9 as diamonds. In ohmic discharges at low density ($\langle n_e \rangle \leq 10^{19}m^{-3}$), T_e ~ 50 eV, and the difference is up to an order of magnitude. The difference then reduces with increasing density, to a factor of 2 for $\langle n_e \rangle = 4 \cdot 10^{19}m^{-3}$. The inferred boundary ion temperatures scale roughly inversely with density in ohmic discharges. Although subject to uncertainties in the sheath transmission factor for beryllium and the calorimetric measurements, they are in

good agreement with the ion temperature pedestals from CXS extrapolations obtained for the same values of power per particle. This behaviour is also seen in recent results from retarding field analyser measurements in the scrape-off layer of DITE, which also show T_i to scale inversely with density at constant ohmic input power[15,16]. In these measurements the local ion temperature measured 2 cm outside the LCFS exceeded the local electron temperature by a factor of 6 at a line average density of $1 \cdot 10^{19} m^{-3}$.

Further evidence is also obtained from passive spectrocopy. Measurements of the Doppler width of a BeIV line using the CXS equipment in ohmic plasmas were obtained for the same discharges as the above probe data and are in good agreement. This is not surprising, since the emission maximum of the line is expected to be several cm inside the LCFS, which is still close enough to provide a good estimate of the pedestal temperature. (The radii of line emission shells depend on ion species and charge states, and electron temperature and density profiles). D_α spectra consist of a 'cold' and a 'warm' component with temperatures of typically 10 and > 70 eV respectively. The warmer component also agrees with previously presented evidence, as seen in fig.9.

Figs 10 and 11 show that the scaling of $T_i(a)$ with power per particle is not merely circumstantial. The measured edge ion temperatures from probes and boundary spectroscopy are plotted versus $P(a)/n_e(a)$, with $n_e(a)$ obtained locally from the same measurements. In the case of the probe measurements (fig.10) the edge density was obtained from the ion saturation current. The scaling with power per particle, $T_i(a) \cong 1.2 \cdot P(a)/n_e(a)$ [eV, MW, $10^{19} m^{-3}$], is observed over a wide range of densities and is clearer than in fig.9, where a nominal boundary density, taken somewhat arbitrarily at $r \cong 0.9a$, was used. This is most probably because the densities at the LCFS and in the bulk plasma are not proportional to each other over the entire operating domain. The densities measured at the LCFS by Langmuir probes are about a factor of 40 lower than volume average bulk plasma densities in most conditions, except at high densities, near the density limit, when a small increase in $\langle n_e \rangle$ results in a large increase in $n_e(a)$[4].

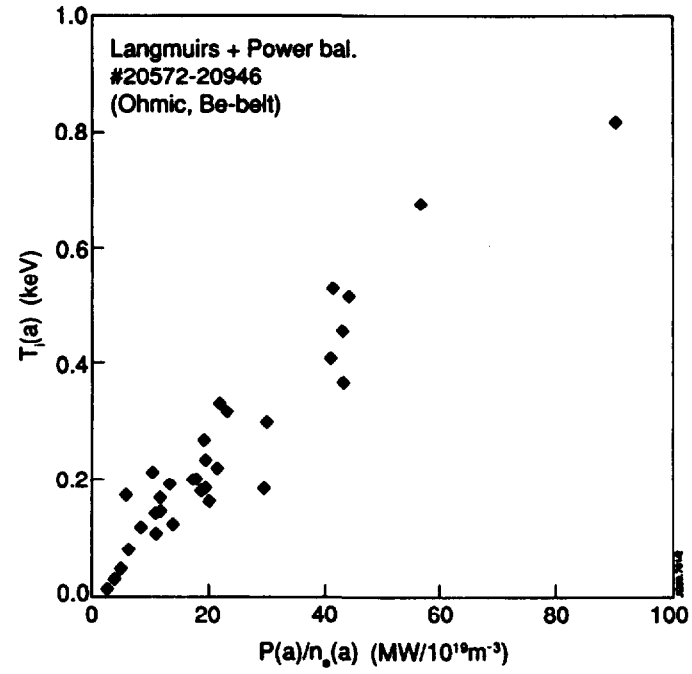

Fig.10 Boundary ion temperature scaling in ohmic Be belt limiter plasmas, as inferred from Langmuir probes in the limiters and calorimetric measurements. The power to the LCFS is normalised to the electron density measured by the probes.

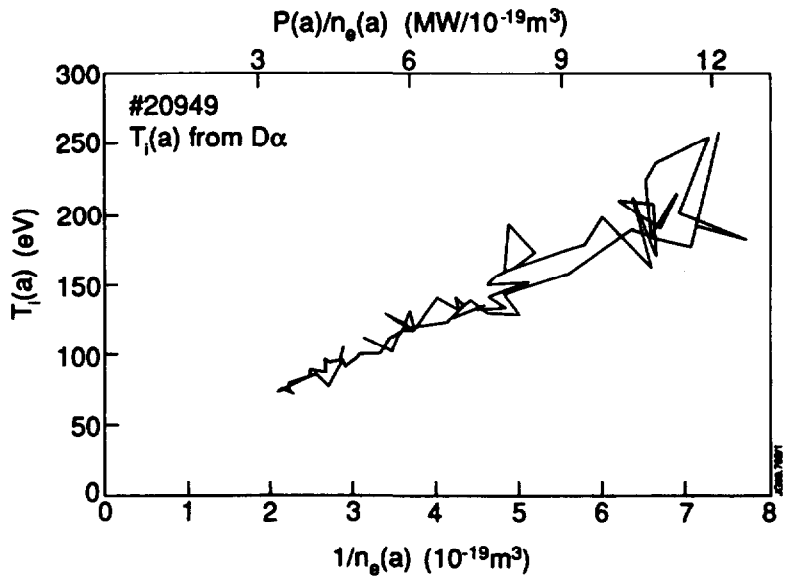

Fig.11 Boundary ion temperature scaling from ohmic Be belt limiter plasma, as inferred from the temperature of the 'warm' component of the D_α edge line. The power to the LCFS is normalised to the electron density measured via the D_α/D_γ line intensity ratio.

In fig.11, showing an example where the density was raised by the injection of a deuterium pellet and then allowed to relax to a low density at roughly constant power to the edge, the boundary density was inferred from D_γ/D_α line ratio measurements. This line ratio is a balance of collisional excitation and radiative decay, and constitutes a sensitive measurement of the electron density at the position of emission[5]. Within errors of the measurement the densities inferred from the 'cold' and the 'warm' components were the same, confirming that the 'warm' component is characteristic of an ion population in the boundary plasma. The origin of the 'warm' D_α emission from the immediate vicinity of the LCFS is also confirmed by the agreement, within a factor of less than two, of the scaling of $T_i(a)$ obtained by the two methods.

The scaling of the boundary ion temperature can be understood from the relationship between particle and heat transport through the boundary. The average kinetic energy loss from the plasma ion population due to an escaping ion is

$$\langle E_i \rangle = \frac{P_i(a)}{\Phi_{out}} , \qquad (2)$$

where P_i is the power in the ion channel, and Φ_{out} is the total flux of escaping ions. The observed scalings with local power/particle at the boundary (figs. 10 & 11) suggests that the local densities and fluxes are proportional. Using the global particle balance $dN_i/dt = \Phi_{out} + \Phi_{in}$, where Φ_{in} is the plasma fuelling rate (including recycling), eq.(2) can be written as

$$\langle E_i \rangle = \frac{P_i(a)}{dN_i/dt - \Phi_{in}} = -\tau_i \frac{P_i(a)}{N_i} . \qquad (3)$$

Inward (outward) fluxes are defined to have a positive (negative) sign. The second equality results from the definition $\tau_i = N_i/(\Phi_{in} - dN_i/dt)$ for the global particle replacement time. From eq.(3), with $N_i = \langle n_i \rangle V$, where $V \cong 110$ m^3 is the JET plasma volume, we expect the scaling

$$\langle E_i \rangle \cong 5\, \tau_i \frac{P_i(a)\ [MW]}{\langle n_i \rangle\ [10^{19} m^{-3}]}\ [keV] . \qquad (4)$$

Direct comparison of experimental observations with eq.(4) is not yet possible because particle replacement times are poorly known. Experimental confinement times obtained from heavy impurity injection experiments in JET L-mode discharges suggest residence times of 0.2 s for particles in the plasma core[24]. In the H-mode particle residence times of 3 seconds or more have been observed, explaining the order-of-magnitude difference in boundary ion temperatures in the two modes of confinement. The particle replacement time is determined mainly by the ionisation mean free path of neutrals entering the plasma[25], and should not be confused with the residence time of particles in the plasma core. The discharges investigated were fuelled by a mixture of beam fuelling and edge fuelling, and the central residence time τ_c of 0.2 s in the L-mode must be taken as an upper bound for τ_i.

If we assume that half of the power to the edge flows in the ion channel, comparison with the observed scalings suggests $<E_i> \cong 6\tau_i/\tau_c T_i(r_p)$ in the H-mode (where $<n_i> \cong n_e(0.9a)$) and typically $<E_i> \cong 3\tau_i/\tau_c T_i(r_p)$, for L-modes (where typically $<n_i> \cong 1.5 \times n_e(0.9a)$). The higher ratio of $<E_i>/T_i(r_p)$ in the H-mode may be due to the contribution of a negative electrostatic trap of potential $-\phi$ set up by non ambipolar ion losses. This case, in which the energy loss per escaping ion is increased by $e\phi$, will be discussed later.

Our interpretation, expressed in eq.(3), that the boundary ion temperatures are established by the power in the ion channel, is further reinforced by the observation that boundary ion temperatures are proportional to the ion temperature gradients measured 10-20 cm inside the LCFS. In H-modes $T_i(r_p) \approx 0.5\ [m] \cdot <dT_i/dr>$, and in limiter plasmas $T_i(r_p) \approx 0.15\ [m] \cdot <dT_i/dr>$, where the brackets denote flux surface averages (fig.12). Such a relationship is to be expected if we balance $P_i(a)$ from eq.(3) with the diffusive ion heat flux in the bulk plasma just inside the density gradient zone, $P_i(r_p) = n_i(r_p)\, \chi_i\, \nabla T_i(r_p)\, S$, with the (weak) assumption $\tau_i \chi_i =$ const, or $D_i \propto \chi_i$, where χ_i and D_i are the ion heat and particle diffusivities, and S the plasma surface area. We can also balance the diffusive heat flux with the power to the boundary from the observed scaling, and use the observed relationship between T_i

and ∇T_i to obtain a typical L-mode estimate for $\chi_i(0.85a) \approx 3$ to 6 m^2/s, decreasing by a factor of 2 to typically ≈ 1.5 to 3 m^2/s during the H-mode. (The range indicates the uncertainty in the ratio $P_i(a)/P(a)$).

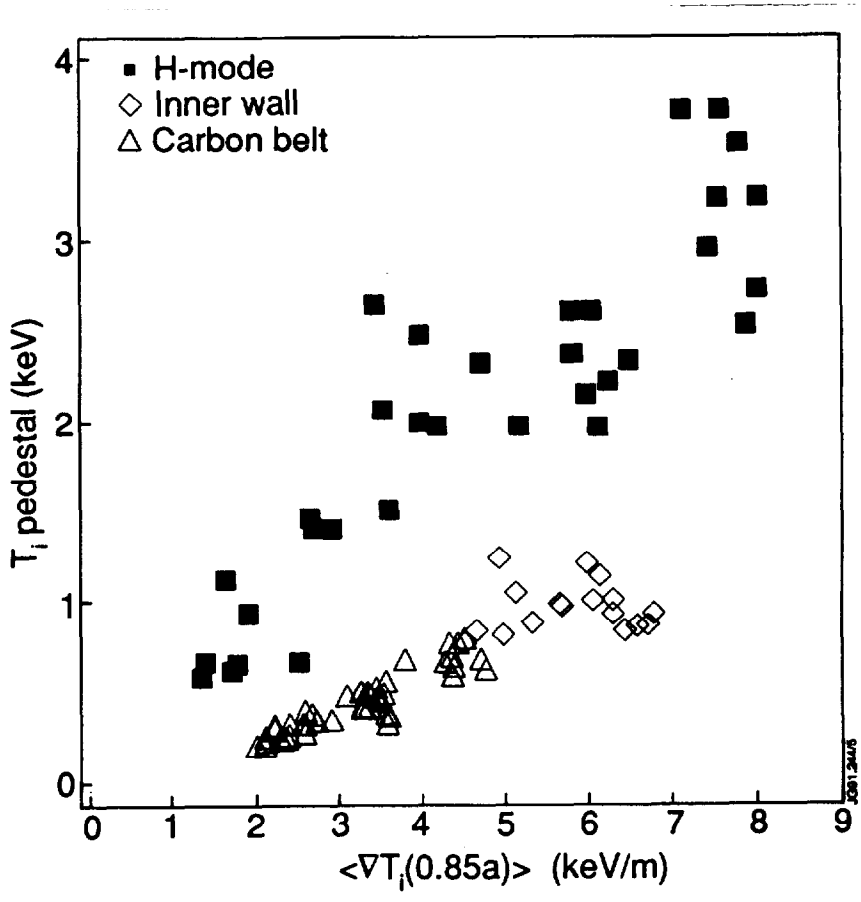

Fig.12 Pedestal ion temperature versus ion temperature gradient (flux surface averaged) at r/a = 0.85 (3 and 4 MA plasmas).

IV) Escape of energetic particles

In many of the CXS measurements on JET, (e.g. as shown in fig.1) edge ion temperatures are such that the LCFS is within less than two poloidal Larmor radii from the observation volume. In such conditions one expects a large number of particles with the required pitch and energy to have orbits intersecting the LCFS. Such particles can be lost to limiters and other obstacles outside the LCFS. Similarly, in the X-point configuration, energetic ions are most easily lost in the vicinity of the poloidal null, where they experience the largest drift away from their 'nominal' flux surfaces. The probe measurements presented in the previous section already indicate that energetic ions reach the LCFS. High ion energies, even outside the LCFS, have however been measured in the plasma boundaries of tokamaks over a period of many years, using a variety of techniques[6-16]. Most of the early results remained unexplained because ion temperature profiles inside the LCFS were unavailable. In JET the escape of energetic particles beyond the LCFS has been confirmed by ion implantation measurements in nickel samples, by results from probes discriminating ions on the basis of their Larmor radius, and from the behaviour of the heat strike zones in the X-point configuration.

Collector probes have been exposed for one or more discharges to measure escaping fast helium ions created by ICRH and in fusion reactions in future D-T experiments. Even in the absence of ICRH they show a distinct peak at a depth corresponding to energies of a few keV. Fig.13 shows a ^4He concentration profile obtained during a single hot ion H-mode discharge, which reached an edge ion and electron temperature pedestals near 2 keV, as determined from passive spectroscopy of a CVI line and ECE. The helium was a residual from a previous conditioning discharge. The typical impact energy suggested by the position of the maximum concentration is 4 keV. This is somewhat higher than the pedestal temperature, as one would expect, since the most energetic ions are the most likely to reach the probe 5 cm away from the LCFS.

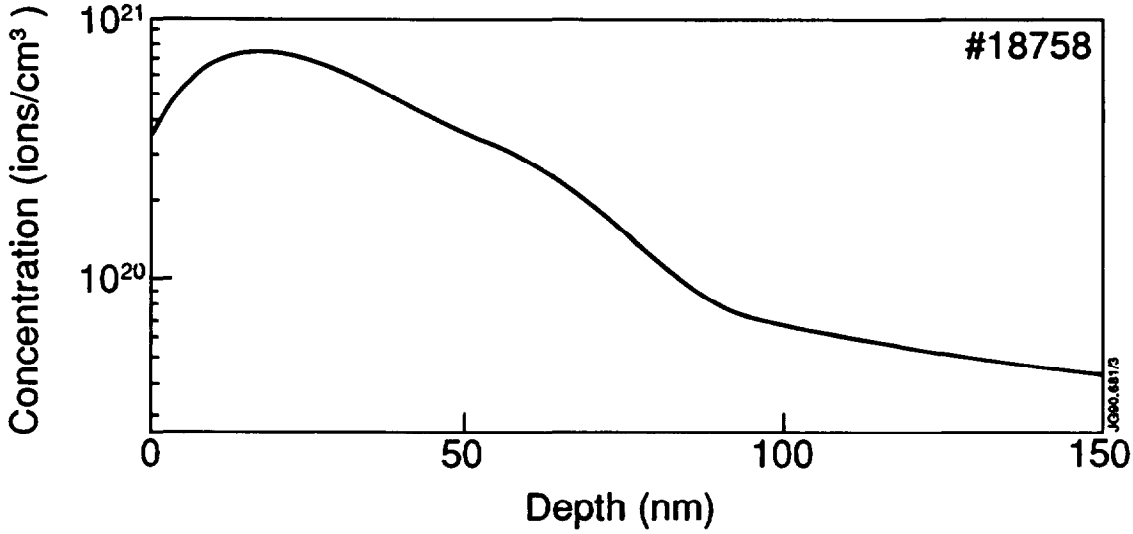

Fig.13 Concentration profile of implanted ^4He in a Ni sample analysed using Secondary Neutral Mass Spectroscopy. The sample was exposed to a hot ion H-mode with a boundary ion and electron temperatures of 2 keV. The maximum corresponds to a 'projected range' of ~4 keV. Discharge no 18757 [27,28].

Similar evidence for carbon and beryllium impurities is obtained from a probe technique capable of discriminating ions on the basis of their Larmor radius[26,27]. The probe consists of a series of collectors mounted in the bottom of slots oriented at different angles to the magnetic field, fig.14. The design of the probe is such that ions can only reach two of the collectors (numbers 0 and 4) directly along the magnetic field. However ions with sufficiently large Larmor radii can reach the remaining collectors. The ratio of the fluxes to the different collectors can be calculated for a specific geometry and charge to mass ratio as a function of ion energy. Results of such a calculation, for $A/Z_i=3$ (e.g. Be^{+3}), using a Monte Carlo technique[27], are shown in fig.15. It is observed that as the ion energy increases fewer ions arrive at collectors 0 and 4 and more come to the collectors at larger angles to the field. The calculations assumed an isotropic Maxwellian energy distribution. An empirical density gradient with an e-folding length $\lambda_n=1.9$ cm, in agreement with Langmuir probe measurements of the electron density in the scrape-off layer, was also assumed. The latter introduces an up/down asymetry due to the combination of helical path and the radial density gradient. For the density e-folding lengths characteristic of JET plasmas, the asymetry between slots +1 and -1 becomes apparent at energies beyond about 3 keV. At 2 keV the flux ratio in slots 0 and 1 is a factor of 4.

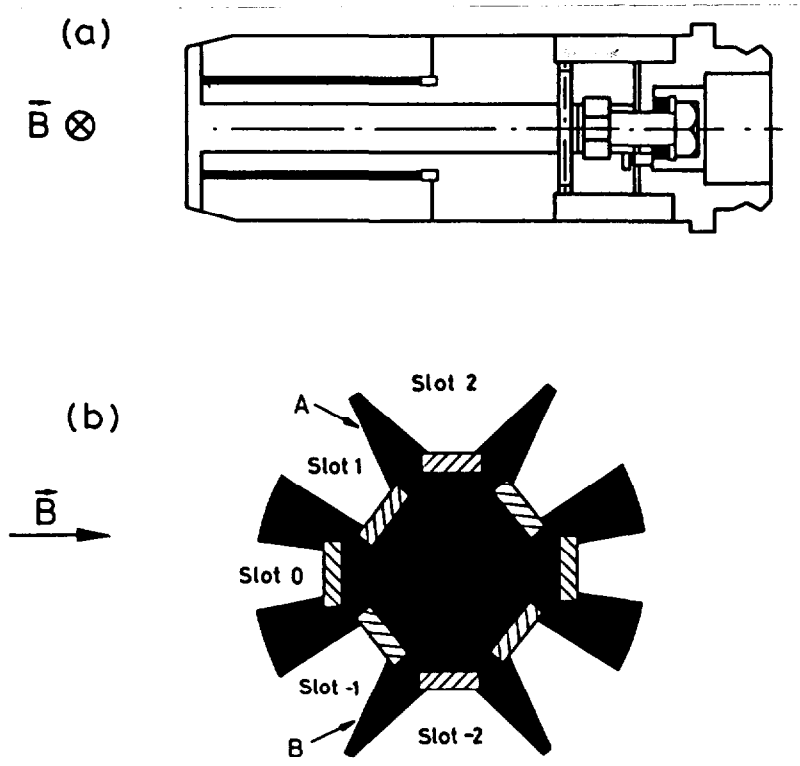

Fig.14 Design of fast ion probe discriminating energies on the basis of Larmor radius. a) Axial section (length 10 cm). b) Cross-section. There are five removable 1× 0.5 cm wide nickel or carbon collectors in each slot. Slot 0 collects low energy particles, while high energy particles can reach 'hidden' slots.

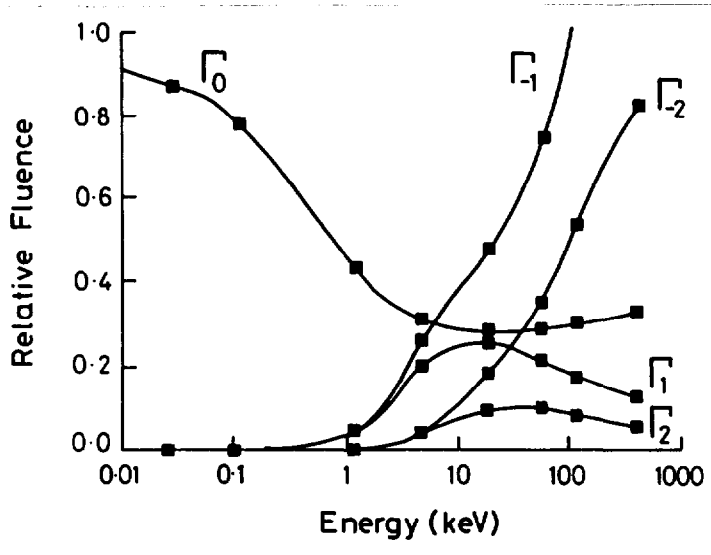

Fig.15 Relative particle flux into the different slots of the fast ion probe as a function of energy. An isotropic Maxwellian ion distribution with $A/Z_i = 3$ (e.g. Be^{+3}) was assumed. (For other species or ionisation stages the horizontal axis is to be rescaled by a factor $(3 \cdot Z_i/A)^{1/2}$.)

The probe was exposed to three similar X-point discharges with 13 MW of NB and RF heating, which underwent a transition to the H-mode for about 1 s. The distance from the probe tip to the LCFS varied between 4 and 6 cm during the discharges. The beryllium and carbon surface concentrations were subsequently analysed by the Nuclear Reaction Analysis technique using the respective (d,p) reactions with a 0.9 MeV deuterium beam. The results of the Be analysis are shown in fig.16. The concentration ratio of slot 0 to slot 1 varies between 4 and 6 as a function of distance from the probe tip. There also is also a clear up/down assymetry. The observed ratios in slots 0 and 1 are not entirely consistent with the observed up/down asymetry if a simple Maxwellian distribution is assumed as in fig.15. This may indicate that the radial e-folding length for energetic ions is different from the

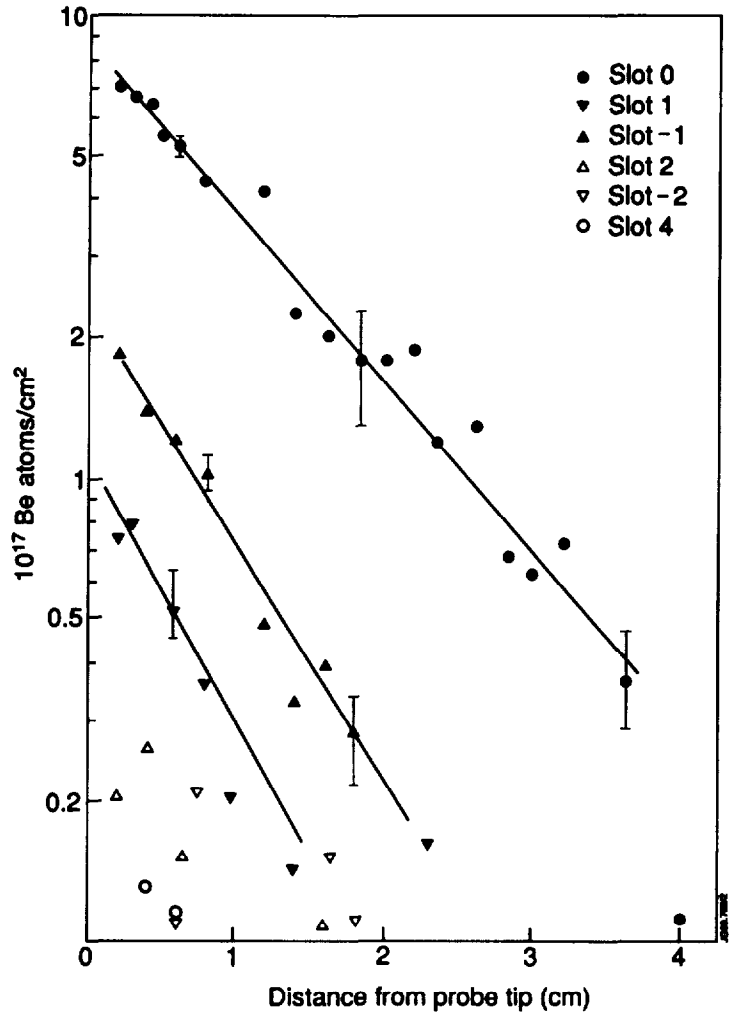

Fig.16 Surface density of Be deposited onto the fast ion probe. The probe was exposed to three X-point discharges with H-mode phases. Probe tip was ~4 cm outside LCFS. The top/bottom assymetry and ratio between slot 0 and hidden slots suggest ion energies between 1 and 10 keV.

one of the background electrons. It should also be noted that edge temperatures vary widely during additional heating, (as seen e.g. in fig.6), and hence the probe results are a superposition ranging from ohmic to H-mode conditions. The ohmic phase is likely to predominately lead to deposition into slot 0, whereas slots 1 and -1 may get most of their impurity deposition only during the much shorter additionally heated phases. In addition it is doubtful whether even the instantaneous ion energy distribution in the scrape-off layer is Maxwellian. These results do however show that ions with energies in the range 1 to 10 keV are present in the boundary plasma beyond the LCFS.

A similar deposition pattern is observed for carbon. The possibility of migration by successive resputtering events (or reevaporation for beryllium) has been suggested as an alternative mechanism for impurities to be deposited into the hidden slots. This however would result in the deposition of low energy ions, and could not lead to the large penetration depths observed in Ni samples, as presented above.

Power deposition and particle fluxes at 3 of the 32 bands of X-point target tiles are monitored using CCD cameras equipped with interchangeable narrow-band wavelength filters. For the observations presented here of the upper X-point tiles, which are made of graphite, these correspond to the D_α line and to low ionisation stages of carbon (CI, CII, CIII). The target tiles are curved in the toroidal direction, allowing us to discriminate between particles incident from the electron and ion drift side. In ohmic plasmas two strike zones are observed, situated on either side of the apex of the tiles, as shown by the shaded areas in fig.17. Line emission from carbon impurities produced at the tile surface extends along the field lines, with the highest ionisation stages showing the largest extent. Emission from neutral carbon is confined to the immediate vicinity of the strike zones, CII and CIII line emission is seen as far as 20 and 35 cm away from them. During auxiliary heating an additional, narrow strike zone nearer to the X-point is observed on the ion drift side of the target plate. It is shown as a black dot in fig.17. The phenomenon had initially been attributed to operation with the X-point outside the free aperture of the vessel[28], as delimited by the apex of the tiles, but

has since been observed with the X-point both inside and outside the vessel free aperture. Fig.18 shows three profiles of surface emissivity at a wavelength of 514 nm, corresponding to a CII line. These profiles were made on the ion drift side along the line AA' at three different times during an additionally heated X-point discharge, which underwent a transition into the H-mode 0.4 s after application of NBI.

The emission from this new strike zone (dubbed 'third strike zone') is primarily thermal, and, unlike the emission from the neighbouring zone (hereafter named first strike zone), increases continuously during the heating phase, and decays slowly thereafter. This emission is detected in all wavelength bands, including at 1 μm, where there are no carbon lines. It is localised to the strike area, and, for modest surface temperatures, no emission is seen along the field lines. The temperatures evaluated from the surface emissivity of the third strike zone can reach 2400 °C, close to the sublimation temperature of carbon[30]. When the tiles reach such temperatures, typically after 1-2 s of high power additional heating, massive influxes of carbon (fig.5c) are the consequence.

The power to the third strike zone is at least one order of magnitude larger than the power to the first zone on the ion drift side during the H-mode. The measured power densities are of the order of 5 kW/cm^2 or about 100 kW for the entire strike zone. Remarkably the localisation of the emission on the target plate shows that, at least as long as the surface temperature remains well below 2400 °C, impurity production at the third strike zone is insignificant. Hence while the third strike zone receives most of the power, it can only get a small fraction of the particle flux to the tile. This observation imposes severe constraints on the range of energies of the incident particles. One can easily verify, that since the particle flux onto the the third strike zone is an order of magnitude (or more) lower than the particle flux on the first strike zone, and at the same time there is an inverse relationship between the heat fluxes, then the average incident ion energy onto the third strike zone must be two (or more) orders of magnitude larger, and the density of incident particles two orders

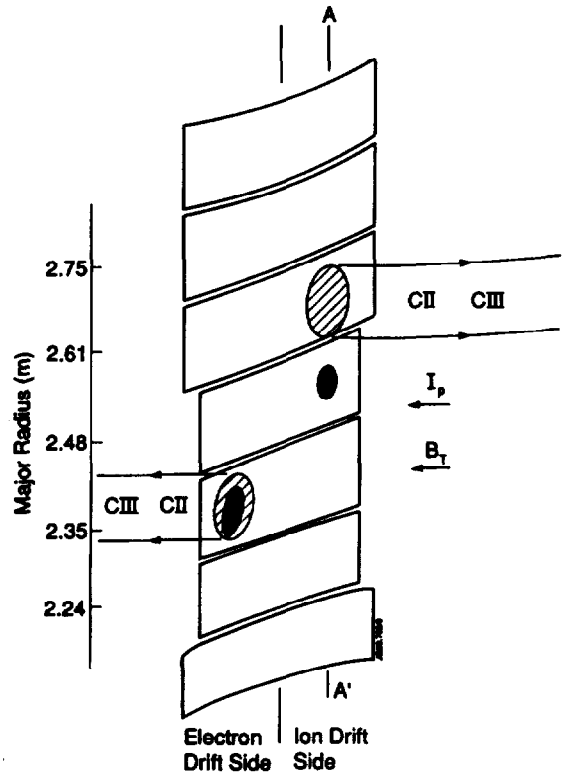

Fig17 Schematic of a band of X-point target tiles. The shaded areas correspond to the strike zones as seen with ohmic heating alone (zones 1 and 2, for ion and electron drift side, as referred to in the main text). During auxiliary heating an additional separate third strike zone (black dot) characterised by a very high ratio of heat to particle flux is observed on the ion drift side. Orbit calculation suggest that energetic ions reaching the electron drift side (black dot in zone 2) do not strike a separate area.

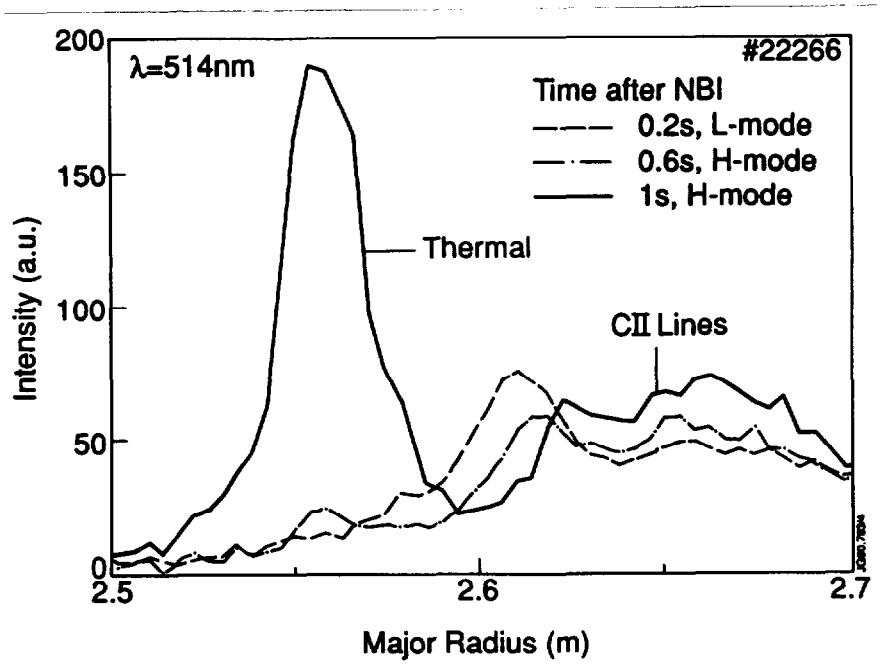

Fig.18 Intensity profiles at a wavelength of 514 nm of target tiles along the line AA' in fig.18 at different times.

of magnitude (or more) lower than on the first strike zone. The electron density and temperature measured by Langmuir probes near strike zone 1, on the apex of the tiles, were about $4 \cdot 10^{19}$ m^{-3} and 40 eV respectively in the example of fig.18. In these conditions the ion-electron collisionality is very high and it is reasonable to assume $T_i \equiv T_e$ at the first strike zone. We conclude that average energy of the particles incident on the third strike zone must be several keV, while their density is probably in the range 10^{17} to 10^{18} m^{-3}. This estimate is consistent with the measured heat flux. At an incident energy of 4 keV, a density of $\sim 2 \cdot 10^{17} m^{-3}$ is required to explain the observed heat load of up to 5 kW/cm^2, corresponding to an ion current density of ~2 A/cm^2 collected by the plate.

Orbit calculations for ions launched inside the LCFS show that on the ion drift side, near the poloidal null, ions are to a large degree separated according to their energies, with the orbits of the highest energy ions coming closest to the X-point[31]. The separation between the zones depends also on the vertical position of the X-point, and is largest when the X-point is near the apex of the tiles, as is the case in many of the X-point configurations produced in JET. The separations observed are consistent with ion energies in the keV range, as also suggested by edge ion temperature measurements by CXS. The same calculations show that the separation is reduced on the electron drift side, low and high energy particles striking roughly the same area. This is also confirmed by the absence of a separate additional strike zone on the electron side, although the power loads are comparable to those on the ion side. If the observed tile bands are representative of the 32 in place, power losses in the form of energetic particles can easily account for most of the ion loss power in additionally heated discharges. In-vessel inspection of the tiles revealed significant erosion damage on the ion drift side of 9 of the 32 tile bands, and on the electron drift side of 29 of the bands. This may however not be a true reflection of the power ratio to the two sides. Enhanced erosion can be expected on the electron drift side because of the spatial overlap of high power/low flux and low power/high flux strike zones. The resulting combination of high surface temperature and high particle flux will lead to larger erosion by Radiation Enhanced

Sublimation (RES)[32] than at any of the two zones on the ion drift side, even if the total heat and particle fluxes are equal.

V) Ion orbit losses.

Ion orbit losses can be very important, as shown in the previous section, and play a key role in H-mode theories[33-36]. The existence of wide ion orbits, intersecting material surfaces outside the LCFS, leads to the formation of a loss region in velocity space. The loss region is typically near the passing-trapped boundary, where orbits are widest, and is characterised by a threshold energy depending on the position in the plasma and the local plasma potential. In the collisionless case, which is applicable to most additionally heated JET plasmas, orbit losses are determined by the rate at which ions are scattered into the loss region. The corresponding loss rate and power density can be written as

$$dn_i(\underline{r})/dt = \gamma(\underline{r})\nu_{ii}(r)n_i(r), \qquad (5)$$

$$p_i(\underline{r}) = \gamma(\underline{r})\nu_{ii}(r)n_i(r)\langle E_i(\underline{r})\rangle, \qquad (6)$$

where $\nu_{ii} \cong 8\cdot10^{-13}Z_i^4\mu^{-1/2}n_iT_i^{-3/2}$ is the ion-ion collision frequency, $\mu=m_i/m_p$, γ is the fraction of collisions leading to an ion loss, and $\langle E_i(\underline{r})\rangle$ the average energy lost when an ion is scattered into the loss region. An exact calculation of (5) would require the formidable task of mapping out the loss region for every point in the discharge. A rough approximation can however be obtained if we note that within a thermal banana width of the LCFS, a collision is likely to lead to the loss of one of the colliding particles, unless it is confined by a potential. We can hence estimate the total losses by multiplying eqs.(5) and (6) by the affected volume, $V_{loss} \cong 2\rho_{\theta i}S$, where $\rho_{\theta i} = 1.02\cdot10^{-4}\sqrt{\mu T_i[eV]}/Z_iB_\theta$ is the ion poloidal Larmor radius, and S the plasma surface. In the limiter configuration B_θ is well defined in terms of the plasma current alone. In the X-point configuration however a clearly larger volume can be affected by the local poloidal null, leading to increased orbit losses.

Using typical JET parameters, B_θ=0.6 T, S $\cong$150 m^2, we obtain for a pure deuterium plasma:

$$dN_i/dt \approx 4 \cdot 10^{24} \langle\gamma\rangle (n_i/10^{19})^2 T_i(r_p)^{-1} \quad (7)$$

$$P_i[W] \approx 6 \cdot 10^5 \langle\gamma\rangle (n_i/10^{19})^2 \langle E_i\rangle / T_i(r_p). \quad (8)$$

In the absence of a confining potential we can take $\langle\gamma\rangle = 1$ and $\langle E_i\rangle / T_i(r_p) = 3/2$. When the ions escape an electrostatic trap, the average loss fraction $\langle\gamma\rangle$ is reduced by the Boltzmann factor $exp(-e\phi(r_p)/T_i(r_p))$. For $e\phi > T_i$, we can take $\langle E_i\rangle \cong e\phi + T_i(1 + T_i/2e\phi)$, to first order in $T_i/e\phi$. This result has been derived for electrons escaping an electrostatic trap in mirror configurations, and predicts that the average energy of a particle is of order T_i and depends only weakly on ϕ[37]. In the absence of a confining potential the orbit loss power can easily exceed the available power in the H-mode, where the density reaches its bulk values within the loss volume. Since the loss power appears to depend only weakly on $e\phi$ for $e\phi(r_p) < T_i(r_p)$, we have to postulate that $e\phi(r_p) > T_i(r_p)$ in the H-mode. An estimate with typical H-mode parameters yields $e\phi/T_i \approx 2$, depending logarithmically on n_i and P_i. A somewhat larger value results when ion losses are enhanced by impurities, or if the above expression for the loss volume is an underestimate in the X-point configuration. We can also get an estimate of the depth of the electrostatic trap if we interpret the steep edge density profiles in the H-mode as due to a Boltzmann distribution of the ions[38]: $e\phi/T_i(r_p) = \ln[n_i(r_p)/n_i(a)] \approx 3$, where r_p is the radius beyond which the gradient steepens. (This is essentially equivalent to the radial force balance in the frame of the ion fluid, integrated between r_p and a, and assuming $\nabla T_i/T_i \ll \nabla n_i/n_i$.) These values also help explaining the gap between $\langle E_i\rangle$ and $T_i(r_p)$ inferred from the power and particle balance in the H-mode, eqs.(2)-(4).

These estimates can be compared to measurements of the edge electric field and ion temperature obtained in machines equipped with high resolution spectroscopic diagnostics[39-43]. The electric field was obtained from the radial force balance balance equation using the measured poloidal rotation velocity and ion pressure. The magnitudes reported are in the range 10-40 kV/m in the vicinity of the LCFS. Preliminary measurements on JET, based on a BeIV transition, have indicated an electric field decreasing by 25 kV/m at the L to H transition, and localised within 10 cm inboard

of the LCFS[44]. Published H-mode results from the DIII-D tokamak show within 2 cm of the LCFS $eE_r \approx 4\ dT_i/dr$ [39], or $eE_r \approx dT_i/dr$ [40,41], measurements on JFT-2M[42] yielded $eE_r \approx 2\ dT_i/dr$ within 2 cm inside the LCFS, while ASDEX results[43] suggest $eE_r \approx 3\ dT_i/dr$ about 4 cm inside the LCFS. These results also suggest, that over the width of the transport barrier, a potential equal to 1 to 4 times the ion temperature pedestal is created. The wide range may reflect differences in the poloidal rotation velocities of the impurities measured. It is presently not clear how these results, obtained with collisional boundary plasmas ($\nu^*_{ii} \geq 10$), can be extrapolated to the low collisionality edge conditions ($\nu^*_{ii} \leq 1$) of JET hot ion H-modes. At low collisionality, ion temperature gradients across the transport barrier, as seen in refs 40-42, as indeed the notion of a local ion temperature defined by a Maxwellian distribution function, may cease to have a meaning. These issues will be addressed by planned high resolution spectroscopic measurements of the JET boundary plasma.

The ion loss current corresponding to the above estimate $J_i\,[A] \approx 6 \cdot 10^5 \langle\gamma\rangle (n_i(r_p)/10^{19})^2/T_i$, can easily exceed 1 kA for $\langle\gamma\rangle = 1$, and compares well with the experimental observations for the third strike zone in the previous section. Such currents, if net, could establish potentials of tens of keV across the loss volume in less than one ms. This may explain the rapid restoration of the transport barrier after ELM's, as apparent from the extremely fast (milliseconds) recovery of edge ion temperatures observed in DIII-D[41]. The ion currents must be balanced by electron currents, and possibly by inward transport of low energy ions from external fuelling or sputtering. Electrons (and low energy ions) can of course not follow the ion loss orbits and must be transported by diffusive processes. (In principle, if reliable transport coefficients in the boundary plasma were available, E_r and $e\phi(r_p)/T_i(r_p)$ could be calculated by balancing these currents.) A sudden reduction of radial electron transport, as appears to happen at the transition to the H-mode, and resulting imbalance of electron and ion currents through the LCFS, would then lead to a rapid deepening (or formation) of the electrostatic trap, followed by the well known H-mode behaviour with increasing density and temperature. The radial electric field may also explain the strong inward convection of impurities in the

vicinity of the separatrix[24]. Recent H-mode theories[34-36] explain the reduction of electron transport by a reduction in the fluctuation level within $\sim 2\rho_\theta$ caused by the sheared poloidal rotation resulting from the electric field set up e.g. by initial ion losses in the L-mode. The suddeness of the transition is described as a bifurcation process by Shaing et al[35,36]. The corresponding poloidal rotation has been observed with high resolution spectroscopy in the above mentioned experiments[39-44]. A sudden reduction in edge turbulence level at the transition into the H-mode has also been observed in several machines[40,41,45], including JET[46].

The observed behaviour suggests a picture of the H-mode transport barrier caused by a strong reduction in electron transport, but where ion confinement is largely electrostatic. Since orbit losses dominate the outer $\sim 2\rho_\theta$, within the LCFS anyway, an improvement of ion diffusivity is not required. An improvement of the magnitude experienced by the electrons is also not likely, since ion orbit widths are comparable to, or wider than, the radial turbulent scale sizes.

Since the observed ion losses can easily set up the edge electric fields established at the L to H-mode transition, the present observations on JET confirm the role of ion orbit losses as a key element in understanding H-mode behaviour. In addition they show that the reduction of electron transport is not sufficient, a reduction of ion losses by the effect of the electric field accross the transport barrier is also required.

VI) Pedestal contribution to global confinement.

The presence of temperature and density pedestals leads to considerable contributions to the stored energies in H-modes as pointed out earlier[21,22]. The pedestal energy was shown to increase roughly linearly with loss power, with a corresponding confinement time $\tau_{ped} \approx 0.4$ s in 3 MA discharges. Since ion temperature profiles were not regularly available, the authors assumed equal ion and electron temperature pedestals. For the densities in their study this assumption was adequate. Thomsen et al[20] defined W_{ped} essentially as $3/2\, k(T_e(r_p)+T_i(r_p))\int(n_e+n_i)dV$. This definition follows naturally from heat transport considerations, if independent heat and particle transport is assumed, but has the disadvantage that the pedestal energy so defined is dependent on the overall density profiles. There are also indications that the edge pressure gradient in H-modes is limited not by transport, but by MHD stability[45,47]. We therefore prefer to adopt the generally more conservative definition of eq.(1), in terms of edge parameters only. In practice the definition adopted makes however little difference. The large majority of H-modes in JET, including the ones studied by Thomsen et al, have flat density profiles, and hence the volume average density is equal to the density just inside r_p. Differences of the order 20 to 40% arise in discharges with peaked density profiles, as shown in fig.7. They include our H-modes with the highest edge ion temperatures, and beam fuelled low-density L-mode discharges. (Larger differences between the two definitions would result for the strongly peaked density profiles produced by the injection of frozen deuterium pellets. Such discharges are not included in this study). A small number of H-modes in the present study had hollow density profiles produced by a strong gas puff. In these cases the definition adopted yields a pedestal energy about 20% higher than would the one used in refs 21 and 22.

Fig.19a shows the plasma energy as a function of loss power, P_{in}-dW/dt for a variety of discharge conditions in JET at a plasma current of 3 MA. They include H-modes with average electron densities in the range $2 - 7{\cdot}10^{19}$ m^{-3}, central electron

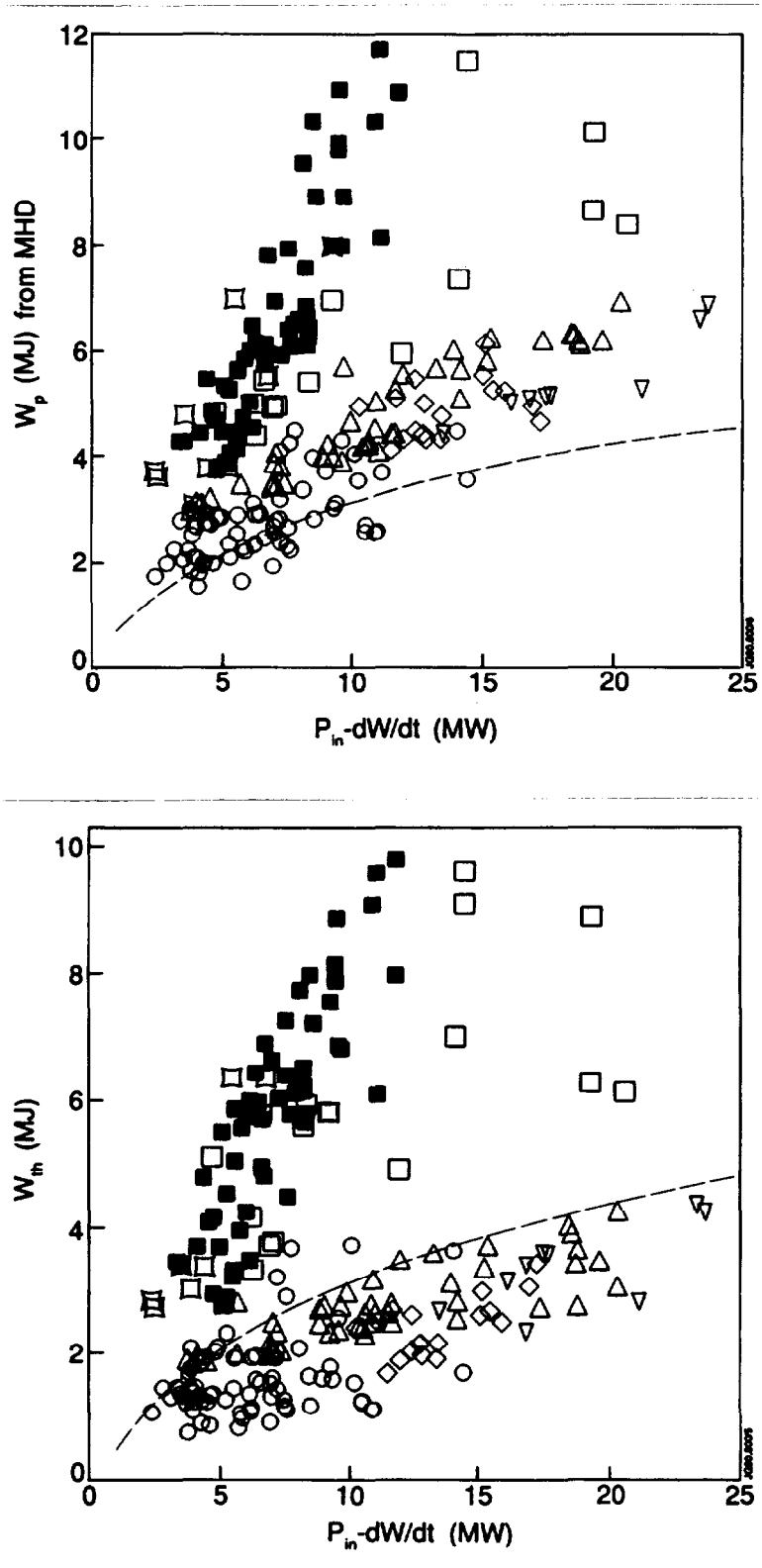

Fig.19 Analysis of plasma stored energy into thermal, pedestal and bulk contributions in 3 MA discharges. Dashed line represents Goldston scaling.
a) Plasma energy from reconstruction of MHD equilibrium.
b) Thermal plasma energy from temperature and density measurements.

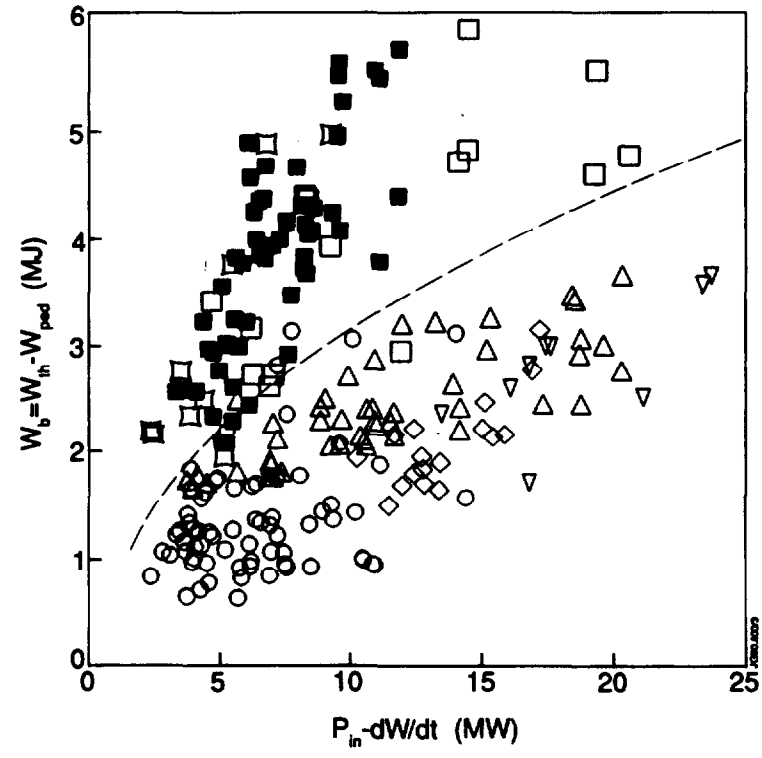

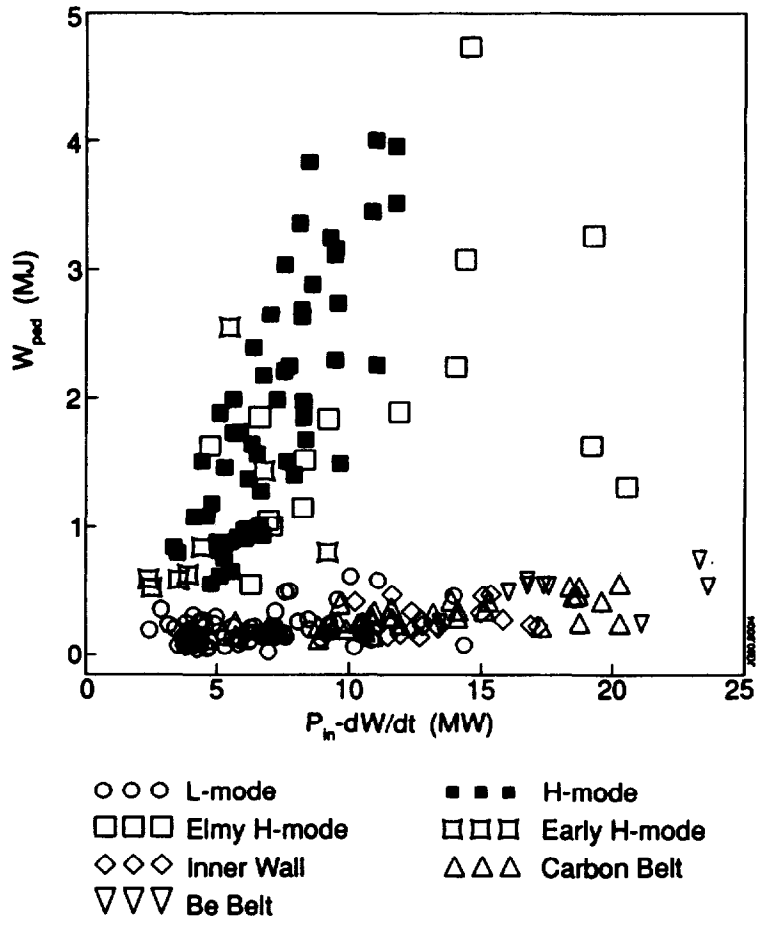

Fig.19 (continued)

c) Pedestal contribution to stored energy.

d) Bulk thermal stored energy.

temperatures in the range 3.5 - 11 keV, central ion temperatures in the range 3 to 27 keV, and ion temperature pedestals up to 4 keV. The largest stored energies were obtained in hot ion H-modes. The limiter and X-point L-mode data contain densities in the range 1 - $5 \cdot 10^{19}$ m^{-3}, central electron temperatures in the range 3 to 9 keV, and central ion temperatures in the range 2.5 to 23 keV. The H-modes were predominantly beam heated. In some of the limiter plasmas a substantial fraction (up to 50%) of the input power was from ICRH. The discharges in this study were selected for the availability and quality of ion and electron temperature and density profile data close enough to the LCFS and may not reflect the best confinement obtained in any mode of operation.

In fig.19b we show the thermal plasma energy obtained from the volume integral of the ion and electron thermal energy densities. The ion density was inferred from the electron density and the impurity density. Impurity densities from CXS were used when available, otherwise they were obtained from visible Bremsstrahlung. Most of the electron temperature and density profiles were obtained from ECE and FIR interferometry. LIDAR Thomson scattering data were used when available. Thermal energies are lower than the corresponding total plasma energies, because of the presence of fast ions from NBI and ICRH. The thermal energy is decomposed into a contribution from the pedestal, W_p, and the bulk, $W_b = W_{th} - W_{ped}$, figs. 19 c & d. In H-modes at 3 MA ion pedestal energies of up to 3 MJ and electron pedestals of up to 2 MJ are obtained for $P_{in} - dW/dt \approx 10$ MW. These results confirm those in refs 21 and 22, and extend them to a wider range of conditions. (The larger scatter is due to the presence of data from all phases of the development of the H-mode). The pedestal accounts for a substantial fraction, but not all, of the improvement of H-mode discharges over L-mode conditions. The best H-modes are hot ion plasmas and are a factor of 3 better than Goldston scaling[48]. In these H-modes improvements in the bulk can contribute as much as the pedestal.

Most of the improvement of bulk plasma confinement appears to result from a reduction of the effective heat conductivity in the edge region, but inside the radius r_p where the sharp edge

gradients occur. This is seen in fig.20 were the the confinement figure of merit $n_e<dT_e/dr> + n_i<dT_i/dr>$, as measured ~15 cm inside the LCFS, is plotted as a function of heat flux q through the magnetic surface at r/a = 0.9. (Flux surface averages were used both for the temperature gradients and the heat flux.) The ion temperature gradients were obtained from the outermost available measurements, situated typically at r/a $\cong$ 0.8a and 0.9a. In the H-mode the effective heat conductivity $\chi_{eff} = (n_e<dT_e/dr>+n_i<dT_i/dr>)/q$ is reduced by an order of magnitude to between 0.5 and 2 m^2/s. This reduction is substantially larger than the reduction by a factor of 2 inferred for χ_i in section III, suggesting that it is mostly due to a decrease in χ_e. The reduced conductivity is mostly a reflection of the higher edge densities in the H-mode, increases in the temperature gradients (particularly of electron temperature) contributing typically a factor of 2. These improvements in the edge region can be related to the observation in the DIII-D tokamak of a zone of reduced heat transport[49], extending gradually inward from the LCFS after the L to H transition, and the gradual reduction of fluctuations inside the plasma after the transition[41].

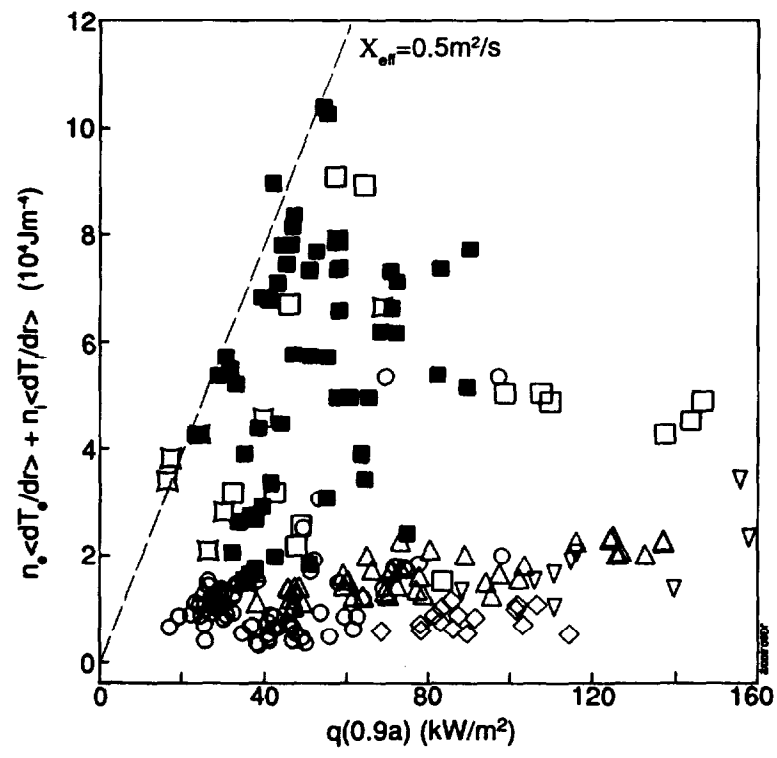

Fig.20 Comparison of effective heat conductivities in H- and L-modes in the edge plasma, 15 cm inside the LCFS.

VII) Pedestal contribution to fusion performance.

In JET H-modes central values of the fusion triple product of up to $10^{21} keVm^{-3}s$ have been obtained (fig.21a). In the presence of a pedestal the central fusion product is however not a good indicator of overall fusion performance. A simple figure of merit is given by the volume average deuteron pressure squared, $\langle p_D^2 \rangle$ (fig.21b). In the temperature range 7 to 25 keV, where $\langle \sigma v \rangle$ scales approximately like T_i^2, $\langle p_D^2 \rangle$ is approximately proportional to the volume average D-T thermal fusion power density.

Fig.21b shows that H-modes perform better by a factor of 10 to 20 than L-modes. Typically 40 to 70 % of the enhancement can be attributed to the formation of a pedestal. Fig.21c shows the pedestal contribution defined as $\langle p_D^2 \rangle_{ped} = \langle p_D^2 \rangle - \langle (p_D - p_D(r_p))^2 \rangle$. In hot ion H-modes the pedestal contributes typically 40% to $\langle p_D^2 \rangle$, and up to 70% in medium to high density H-modes, which have broader temperatures profiles due to poorer beam penetration.

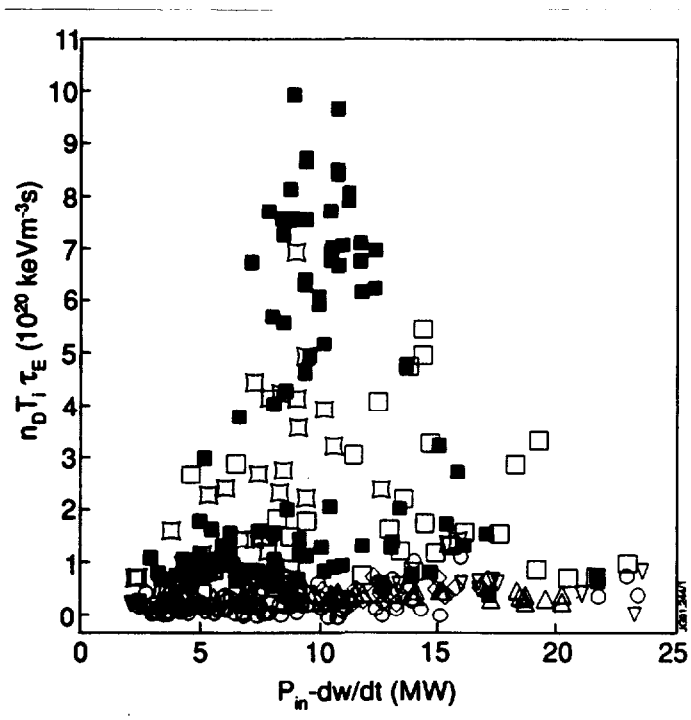

Fig.21 Fusion performance in JET versus net input power in 3 and 4 MA discharges. a) Central fusion product.

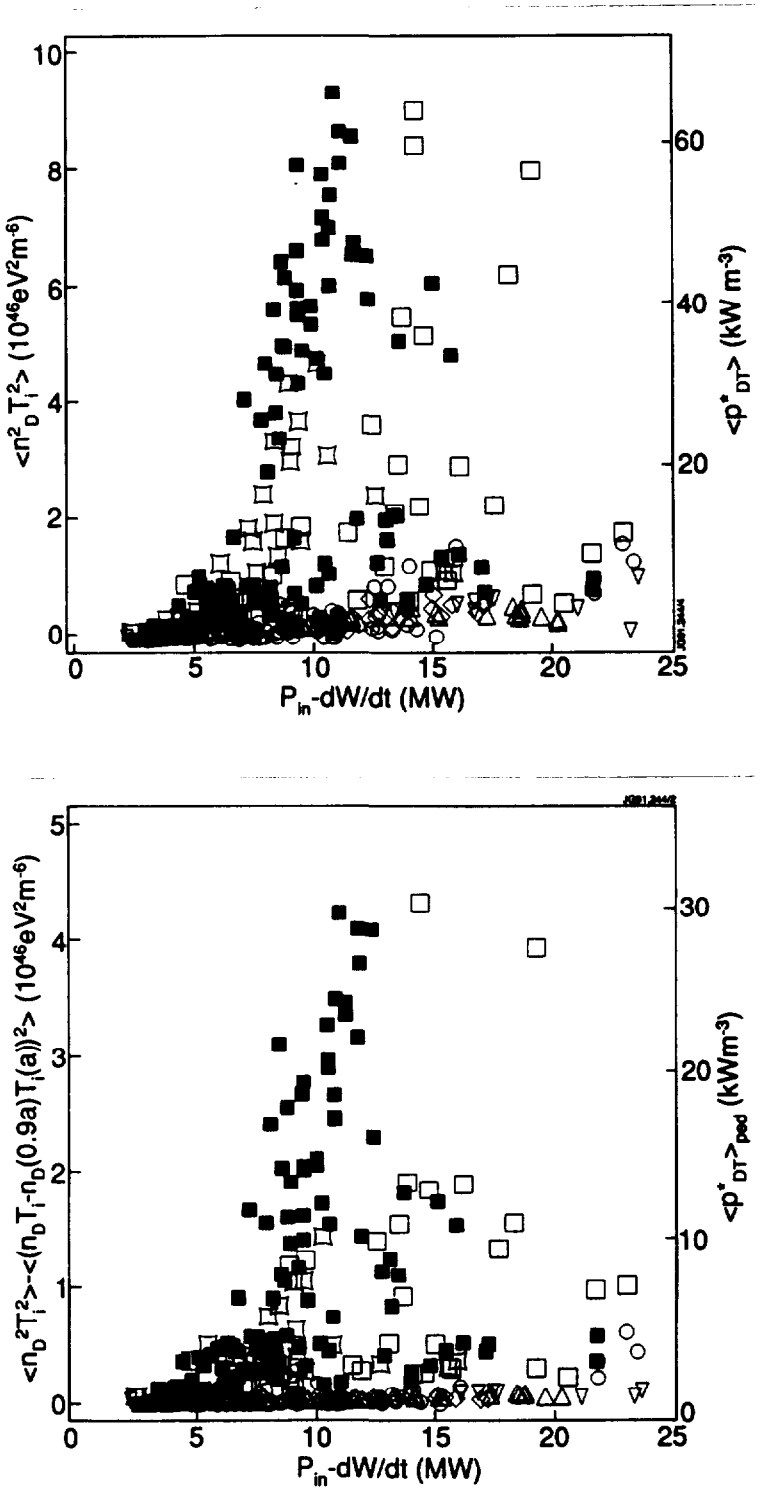

Fig.21 Fusion performance in JET (continued).

b) Volume average deuteron pressure squared. The right vertical axis is the approximate thermal D-T fusion power density produced for $T_i > 7$ keV throughout the profile, if half of the deutrium was replaced by tritium.

c) Pedestal contribution to volume average deuteron pressure squared.

The pedestal contribution in materially limited plasmas is in the range 5 to 15 %. (An alternative definition of the pedestal contribution, based on the pedestal temperature only, $\langle p_D^2 \rangle_{ped} = \langle p_D^2 \rangle - \langle n_D^2 (T_i - T_i(r_p))^2 \rangle$ would result, for most JET profiles, in attributing a slightly larger fraction of the overall performance to the pedestal.)

In reactor conditions the existence of pedestals with $T_i(a) \geq 7$ keV can lead to a substantial increase in confined alpha-particle power and a corresponding reduction of the ignition threshold, despite prompt losses from the periphery. In the temperature range of interest, the pedestal contribution to the power $P_{\alpha c}$ of confined alphas is proportional to

$$P_{\alpha c} \propto \langle p_D^2 \rangle_{ped} - p_D^2(r_p) \cdot V_{loss}/V \,, \qquad (9)$$

where p_D is the the fuel pressure, V_{loss} is the volume from which alpha particles are lost promptly or without significant thermalisation. For an ITER sized device[50] $V_{loss}/V = 0.3$ can be expected. Assuming pressure profiles similar to those in JET, it is easily seen that only a small fraction of the alphas contributed by the pedestal will be lost.

The absolute pedestal pressure, and so its relative importance, may be expected to be larger in reactor conditions than in JET. This becomes apparent upon inspection of eq.(3). Although little is known on the scaling of particle replacement time with device size, it is generally accepted that it will follow the energy confinement time. For ITER we may assume that τ_i increases by a factor of 5, roughly in proportion with the plasma volume. Since however the auxiliary heating power envisaged for ITER is also a factor of 5 higher than on JET, eq.(3) suggests that in the H-mode ion temperature pedestals of the order of 10 keV may be obtained at edge densities of $5 \cdot 10^{19} m^{-3}$. Such edge pressures would correspond to $\beta \approx 2.5\%$ in ITER, and would make a considerable contribution towards ignition. The resulting high reactivity in the periphery may however be a cause for concern if the corresponding heat load is spatially concentrated, as is the case for ripple trapped alpha particle losses[51].

VIII) Summary and discussion.

The results of this study have established a connection between the ion temperature 'pedestals' observed by CXS, and the detection, by a variety of probe techniques, of ions with energies in the keV range in the scrape-off plasma. These energetic ions can be explained by orbit losses from the main plasma, where temperatures of up to 5 keV have been measured in H-modes within 10 cm of the last closed flux surface. Pedestal ion temperatures in the H-mode scale like power per particle, $T_i(r_p) \leq 1.3 \cdot P(a)/n_e(0.9a)$ [keV, MW/10^{19} m^{-3}]. Boundary ion temperatures in limiter discharges also follow a scaling with power per particle, but are an order of magnitude lower than the H-modes. This scaling can be understood from the relationship between ion energy and particle fluxes through the boundary, $T_i(r_p) \propto \langle E_i \rangle = \tau_i P_i(a)/N_i$.

Although probe measurements of ions in the scrape-off layer are still in an early stage, having no temporal resolution, and only a coarse energy resolution, they clearly show that keV ions escape beyond the LCFS. They suggest a complex picture of the scrape-off plasma where energetic escaping ions coexist with a background of lower energy ions from the ionisation of fuel and sputtered impurities, and call for time resolved measurements of the local ion velocity distribution functions. Escape energies in the keV range have also been inferred from the power to particle flux ratio at the X-point heat strike zones, and their location with respect to the X-point. They show that ion orbit losses account for most of the loss power in the ion channel, and also show a decoupling of heat and particle fluxes into the divertor region. The observed magnitudes of ion power and particle losses are consistent with our estimates for orbit losses, and if net, could set up electric fields of tens of kV/m across the transport barrier in less than one millisecond.

The observed ion losses can easily account for the formation of electric fields as observed at the L to H transition in the boundary of several tokamaks[39-43] including JET[44], and hence confirm their potential role in establishing the H-mode. Orbit losses are also a

key element in recent H-mode theories, which explain the formation of the transport barrier by a reduction in turbulent transport caused by the sheared poloidal rotation induced by the edge electric field[34-36]. Our analysis indicates that a reduction of electron transport through the transport barrier, although necessary, is not sufficient, a reduction of ion orbit losses by the confining effect of the electric field accross the transport barrier is also required.

In the H-mode the pressure pedestals established across the transport barrier contribute typically 40% to the stored thermal energy. Although significant, this is generally only about half of the overall improvement of H-modes over L-modes, which have negligible pedestal energies. The remaining improvements occur throughout the cross section, but most noticably near the edge. At r/a=0.85, χ_{eff} drops from typically 10 m^2/s in the L-mode to about 1 m^2/s in the H-mode, mostly as a result of improved electron confinement. The recent H-mode theories[34-36] do not explain the improvements of confinement in the bulk of the discharge.

The results from the JET device suggest that the entire volume of a tokamak reactor plasma can be taken to thermonuclear temperatures, with edge pressures sufficient to make a significant contribution to the overall fusion reactivity. In JET H-modes the pedestal contribution to the volume average of the deuteron pressure squared (which is proportional to the fusion power density for $T_i > 7$ keV) is already 40 to 70%. The volume average deuteron pressure squared in L-modes is 10 to 20 times less than in H-modes.

In reactor conditions the deposition of most of the ion power in the form of particles with high energies of the order of 10 keV is favourable from the point of view of impurity production by sputtering because of the correspondingly low particle fluxes, and the lower sputtering yields at high energies[32,52]. Target surfaces should however be designed with ion orbits in mind in order to avoid local overheating. Present JET experience suggests that target surfaces close to the X-point are most unfavourable because escaping ions are most 'focussed' near the poloidal null.

Impurity accumulation and poor ash exhaust are generally considered as the major drawbacks of an H-mode reactor, and can preclude steady-state operation. The relatively modest particle replacement times ($\tau_i \sim 3\tau_E$) in many of the JET high performance H-modes, and the demonstration of an H-mode in DIII-D[53] with a density maintained constant by ELM activity for 10 s, suggest that these problems of H-mode operation can be overcome. It is also important to note that ELMs do not significantly depress the time averaged boundary ion temperature or pressure, leaving intact its contribution to the overall fusion reactivity. The scaling of boundary ion temperatures suggests that the edge ion pressure, and hence its contribution to the overall fusion reactivity may substantially increase in a reactor sized device, and make ignition in the H-mode easier than generally anticipated.

Acknowledgements

It is a pleasure to thank our many colleages of the JET team who have made freely available the data on electron temperature, electron density, plasma energy and magnetic topology, used in this study alongside our measurements of ion temperatures and energies. We also acknowledge useful and stimulating discussions with J Callen, K Thomsen, R Pitts, N Hawkes, K Borrass, S Clement and T Tagle.

References

[1] F W Wagner, G Becker, K Behringer, D Campbell et al, Phys. Rev. Lett. **49**, (1982) 1408.

[2] M Keilhacker, G Becker, K Bernhardi, A Eberhagen, M ElShaer et al, Plasma Phys. Contr. Fusion **26**, (1984), 49.

[3] F Wagner, G Fussmann, T Grave, M Keilhacker, M Kornherr et al, Phys.Rev.Lett **53**, (1984), 1453.

[4] S K Erents, S Clement, P J Harbour, M von Hellermann, L de Kock et al, 17th Eur Conf Contr Fusion Plasma Heating, Amsterdam, ECA 14B, III, (1990), 1385.

[5] M F Stamp, H P Summers, 17th Eur Conf Contr Fusion Plasma Heating, Amsterdam, ECA 14B, III, (1990), 1377.

[6] G M McCracken, S A Cohen, H F Dylla, S M Rossnagel, C W Magee et al, 9th EPS Oxford, 1979. Also PPPL report no 1569, (1979).

[7] W R Wampler, S T Picaux, S A Cohen, H F Dylla, G M McCracken, S Rossnagel, J. Nucl. Mats., **85 & 86**, (1979) 983.

[8] P Staib, J Nucl Mats **93 & 94**, (1980) 351.

[9] S K Erents, E S Hotston, G M McCracken, C J Sofield, J Shea, J Nucl Mats, **93 & 94**, (1980) 115.

[10] W R Wampler, D K Brice, C W Magee, J. Nucl. Mater. 102 (1981) 304.

[11] G Staudenmaier, P Staub, W Poschenrieder, J. Nucl., Mater., **93 & 94**, (1980) 121.

[12] S K Erents, P C Stangeby, J. Nucl. Mater., **111 & 112**, (1982), 165.

[13] D M Manos, R Budny, T Satake, S A Cohen, J. Nucl. Mater. **111 & 112**, (1982) 130.

[14] A S Wan, PhD Thesis, Dept of Nuclear Engineering, Masachussets Institute of Technology, PFC/RR-8613 (1986).

[15] R A Pitts, G F Matthews, G M McCracken, S J Fielding, 16th Eur Conf Contr Fusion Plasma Physics, Venice, ECA 13B, III (1989), 955.

[16] R A Pitts, 'Ion energy, sheath potential and secondary electron emission in the tokamak edge', PhD Thesis, University of London. Also private communication (1990).

[17] M G von Hellermann W Mandl, H P Summers, H Weisen, A Boileau et al, Rev. Sci. Instrum. **61** (1990), 3479.

[18] H Weisen, M von Hellermann, A Boileau et al, Nucl. Fusion **29**, (1989) 2187.

[19] A Boileau, M von Hellermann, L D Horton, J Spence, H P Summers, Plasma Phys. Contr. Fusion **31**, (1989) 779.

[20] The JET Team (presented by D J Campbell), Plasma Phys. Contr. Fusion **32**, (1990) 949.

[21] K Thomsen, J D Callen, J P Christiansen, J G Cordey, M Keilhacker et al, 16th Eur Conf Contr Fusion Plasma Physics, Venice, ECA 13B, I (1989), 233.

[22] M L Watkins, B Balet, V P Bhatnagar, J G Cordey, G W Hammet et al, Plasma Phys Contr Fusion **31**, (1989) 1713.

[23] The JET Team (presented by P E Stott), Phys. Fluids B **3** (1991) (to be published).

[24] D Pasini, B Denne-Hinnov, R Gianella, N Hawkes, L Lauro Taroni, et al, 18th Eur Conf Contr Fusion Plasma Physics, Berlin (1991) *(in preparation)*

[25] P C Stangeby and G McCracken, Nucl. Fusion **30** (1990) 1225.

[26] R A Pitts, G M McCracken, G F Matthews, J. Nucl. Mater. 162-164 (1989) 568.

[27] E V Carruthers, J Zhu, P C Stangeby, G M McCracken, J P Coad et al, 9th PSI, Bournemouth, May 1990. (to be published in J. Nucl. Mater.)

[28] B Balet, D A Boyd, D J Campbell, C D Challis, J P Christiansen et al, Nucl. Fusion **30**, (1990) 2029.

[29] D P O'Brien, M A Kovanen, R Reichle, W Core, E Lazzaro et al, 17th Eur Conf Contr Fusion Plasma Heating, Amsterdam, ECA **14B** part I (1990), 251.

[30] R Reichle, D D R Summers, M F Stamp, 9th PSI, Bournemouth, May 1990, to be published in J. Nucl. Mater.(1991)

[31] D R Summers et al, Proc 18th Eur Conf Contr Fusion Plasma Heating, Berlin 1991. *(in preparation)*

[32] V Philipps, E Vietzke, H Trinkaus, 4th Int. Conf. Fusion Reactor Mat., Kyoto, Japan, Dec 1989.

[33] F L Hinton, Nucl. Fusion **25**, (1985) 1457.

[34] K C Shaing and E C Crume, Jr, Phys. Rev. Lett **63**, (1989) 2369.

[35] K C Shaing, E C Crume, W A Houlberg, Phys. Fluids B**2**, (1990) 1492.

[36] H Biglari, P H Diamond, P W Terry, Phys. Fluids B**2**, (1990) 1.

[37] V P Pastukhov, Nucl. Fusion **14**, (1974) 3.

[38] V E Golant, A P Zhilinsky, I E Sakharov, 'Fundamentals of Plasma Physics', chap.4, S C Brown editor, Wiley & Sons, 1980.

[39] R J Groebner, K H Burrell, R P Seraydarian, Phys. Rev. Lett. **64**, (1990), 3015.

[40] R J Groebner, W A Peebles, K H Burrell, T N Carlstrom, P Gohill et al, IAEA CN-53/A-6-4, Washington DC (1990). Also GA report GA-A20272.

[41] E J Doyle, R J Groebner, K H Burrell, P Gohill, T Lehecka et al, 'Modifications in Turbulence and Edge Electric Fields at the L-H Transition in DIII-D', to be published in Phys. Fluids (1991).

[42] K Ida, S Hidekuma, Y Miura, T Fujita, M Mori et al, Phys. Rev. Lett. **65**, (1990) 1364.

[43] A R Field, G Fussmann, J V Hofmann, 'Measurement of the Radial Electric Field in the ASDEX Tokamak', report IPP III/165 (1990), Max-Planck-Institut fuer Plasmaphysik, D-8046 Garching.

[44] N Hawkes, JET, Private communication, (1991).

[45] ASDEX Team, Nucl. Fusion **29**, 1989.

[46] P A Duperrex, P Cripwell, A W Edwards, R D Gill, R S Granetz et al, 14th Eur Conf Contr Fusion Plasma Physics, Madrid (1987), ECA **11D**, Vol I, 93.

[47] P Gohil, M A Mahdavi, L Lao, K H Burrell, M S Chu et al, Phys. Rev. Lett. **61**, (1988) 1603.

[48] R J Goldston, Plasma Phys. Contr. Fusion **26**, (1984) 87.

[49] K H Burrell, R J Groebner, T S Kurki-Suonio, T N Carlstrom et al, IAEA CN-53/A-2-3, Washington DC (1990). Also GA report A20277.

[50] J R Gilleland, Yu A Sokolov, K Tomabechi, R Toschi, Nucl. Fusion **29** (1989), 1191.

[51] D E Post, K Borrass, J D Callen, S A Cohen, J G Cordey et al, ITER documentation series no **21** (1990), 2.4-1.

[52] J Roth, in 'Physics of Plasma-Wall Interactions in Controlled Fusion', NATO ASI Series B, Vol. 131, Plenum Press, Edited by D E Post and R Behrisch (1984).

[53] R D Stambaugh et al, IAEA CN-53/A-1-4, Washington DC (1990).

APPENDIX 1.

THE JET TEAM

JET Joint Undertaking, Abingdon, Oxon, OX14 3EA, U.K.

J.M.Adams[1], F.Alladio[4], H.Altmann, R.J.Anderson, G.Appruzzese, W.Bailey, B.Balet, D.V.Bartlett, L.R.Baylor[24], K.Behringer, A.C.Bell, P.Bertoldi, E.Bertolini, V.Bhatnagar, R.J.Bickerton, A.Boileau[3], T.Bonicelli, S.J.Booth, G.Bosia, M.Botman, D.Boyd[31], H.Brelen, H.Brinkschulte, M.Brusati, T.Budd, M.Bures, T.Businaro[4], H.Buttgereit, D.Cacaut, C.Caldwell-Nichols, D.J.Campbell, P.Card, J.Carwardine, G.Celentano, P.Chabert[27], C.D.Challis, A.Cheetham, J.Christiansen, C.Christodoulopoulos, P.Chuilon, R.Claesen, S.Clement[30], J.P.Coad, P.Colestock[6], S.Conroy[13], M.Cooke, S.Cooper, J.G.Cordey, W.Core, S.Corti, A.E.Costley, G.Cottrell, M.Cox[7], P.Cripwell[13], F.Crisanti[4], D.Cross, H.de Blank[16], J.de Haas[16], L.de Kock, E.Deksnis, G.B.Denne, G.Deschamps, G.Devillars, K.J.Dietz, J.Dobbing, S.E.Dorling, P.G.Doyle, D.F.Düchs, H.Duquenoy, A.Edwards, J.Ehrenberg[14], T.Elevant[12], W.Engelhardt, S.K.Erents[7], L.G.Eriksonn[5], M.Evrard[2], H.Falter, D.Flory, M.Forrest[7], C.Froger, K.Fullard, M.Gadeberg[11], A.Galetsas, R.Galvao[8], A.Gibson, R.D.Gill, A.Gondhalekar, C.Gordon, G.Gorini, C.Gormezano, N.A.Gottardi, C.Gowers, B.J.Green, F.S.Griph, M.Gryzinski[26], R.Haange, G.Hammett[6], W.Han[9], C.J.Hancock, P.J.Harbour, N.C.Hawkes[7], P.Haynes[7], T.Hellsten, J.L.Hemmerich, R.Hemsworth, R.F.Herzog, K.Hirsch[14], J.Hoekzema, W.A.Houlberg[24], J.How, M.Huart, A.Hubbard, T.P.Hughes[32], M.Hugon, M.Huguet, J.Jacquinot, O.N.Jarvis, T.C.Jernigan[24], E.Joffrin, E.M.Jones, L.P.D.F.Jones, T.T.C.Jones, J.Källne, A.Kaye, B.E.Keen, M.Keilhacker, G.J.Kelly, A.Khare[15], S.Knowlton, A.Konstantellos, M.Kovanen[21], P.Kupschus, P.Lallia, J.R.Last, L.Lauro-Taroni, M.Laux[33], K.Lawson[7], E.Lazzaro, M.Lennholm, X.Litaudon, P.Lomas, M.Lorentz-Gottardi[2], C.Lowry, G.Magyar, D.Maisonnier, M.Malacarne, V.Marchese, P.Massmann, L.McCarthy[28], G.McCracken[7], P.Mendonca, P.Meriguet, P.Micozzi[4], S.F.Mills, P.Millward, S.L.Milora[24], A.Moissonnier, P.L.Mondino, D.Moreau[17], P.Morgan, H.Morsi[14], G.Murphy, M.F.Nave, M.Newman, L.Nickesson, P.Nielsen, P.Noll, W.Obert, D.O'Brien, J.O'Rourke, M.G.Pacco-Düchs, M.Pain, S.Papastergiou, D.Pasini[20], M.Paume[27], N.Peacock[7], D.Pearson[13], F.Pegoraro, M.Pick, S.Pitcher[7], J.Plancoulaine, J-P.Poffé, F.Porcelli, R.Prentice, T.Raimondi, J.Ramette[17], J.M.Rax[27], C.Raymond, P-H.Rebut, J.Removille, F.Rimini, D.Robinson[7], A.Rolfe, R.T.Ross, L.Rossi, G.Rupprecht[14], R.Rushton, P.Rutter, H.C.Sack, G.Sadler, N.Salmon[13], H.Salzmann[14], A.Santagiustina, D.Schissel[25], P.H.Schild, M.Schmid, G.Schmidt[6], R.L.Shaw, A.Sibley, R.Simonini, J.Sips[16], P.Smeulders, J.Snipes, S.Sommers, L.Sonnerup, K.Sonnenberg, M.Stamp, P.Stangeby[19], D.Start, C.A.Steed, D.Stork, P.E.Stott, T.E.Stringer, D.Stubberfield, T.Sugie[18], D.Summers, H.Summers[20], J.Taboda-Duarte[22], J.Tagle[30], H.Tamnen, A.Tanga, A.Taroni, C.Tebaldi[23], A.Tesini, P.R.Thomas, E.Thompson, K.Thomsen[11], P.Trevalion, M.Tschudin, B.Tubbing, K.Uchino[29], E.Usselmann, H.van der Beken, M.von Hellermann, T.Wade, C.Walker, B.A.Wallander, M.Walravens, K.Walter, D.Ward, M.L.Watkins, J.Wesson, D.H.Wheeler, J.Wilks, U.Willen[12], D.Wilson, T.Winkel, C.Woodward, M.Wykes, I.D.Young, L.Zannelli, M.Zarnstorff[6], D.Zasche[14], J.W.Zwart.

PERMANENT ADDRESS

1. UKAEA, Harwell, Oxon. UK.
2. EUR-EB Association, LPP-ERM/KMS, B-1040 Brussels, Belgium.
3. Institute National des Récherches Scientifique, Quebec, Canada.
4. ENEA-CENTRO Di Frascati, I-00044 Frascati, Roma, Italy.
5. Chalmers University of Technology, Göteborg, Sweden.
6. Princeton Plasma Physics Laboratory, New Jersey, USA.
7. UKAEA Culham Laboratory, Abingdon, Oxon. UK.
8. Plasma Physics Laboratory, Space Research Institute, Sao José dos Campos, Brazil.
9. Institute of Mathematics, University of Oxford, UK.
10. CRPP/EPFL, 21 Avenue des Bains, CH-1007 Lausanne, Switzerland.
11. Risø National Laboratory, DK-4000 Roskilde, Denmark.
12. Swedish Energy Research Commission, S-10072 Stockholm, Sweden.
13. Imperial College of Science and Technology, University of London, UK.
14. Max Planck Institut für Plasmaphysik, D-8046 Garching bei München, FRG.
15. Institute for Plasma Research, Gandhinagar Bhat Gujat, India.
16. FOM Instituut voor Plasmafysica, 3430 Be Nieuwegein, The Netherlands.
17. Commissiariat à L'Energie Atomique, F-92260 Fontenay-aux-Roses, France.
18. JAERI, Tokai Research Establishment, Tokai-Mura, Naka-Gun, Japan.
19. Institute for Aerospace Studies, University of Toronto, Downsview, Ontario, Canada.
20. University of Strathclyde, Glasgow, G4 ONG, U.K.
21. Nuclear Engineering Laboratory, Lapeenranta University, Finland.
22. JNICT, Lisboa, Portugal.
23. Department of Mathematics, Univeristy of Bologna, Italy.
24. Oak Ridge National Laboratory, Oak Ridge, Tenn., USA.
25. G.A. Technologies, San Diego, California, USA.
26. Institute for Nuclear Studies, Swierk, Poland.
27. Commissiariat à l'Energie Atomique, Cadarache, France.
28. School of Physical Sciences, Flinders University of South Australia, South Australia SO42.
29. Kyushi University, Kasagu Fukuoka, Japan.
30. Centro de Investigaciones Energeticas Medioambientales y Techalogicas, Spain.
31. University of Maryland, College Park, Maryland, USA.
32. University of Essex, Colchester, UK.
33. Akademie de Wissenschaften, Berlin, DDR.

CR 88.49.1A